International Journal of Machine Tools & Manufacture 204 (2025) 104235

Contents lists available at ScienceDirect

International Journal of Machine Tools and Manufacture

journal homepage: www.elsevier.com/locate/ijmactool

Research Article

Understanding thermal-mechanical variations and resulting joint integrity of pressure-controlled linear friction welding of thin-steel sheets

Rishabh Shotri [a,*], Takuya Miura [a], Peihao Geng [a,b], Yoshiaki Morisada [a], Kohsaku Ushioda [a], Hidetoshi Fujii [a,**]

[a] Joining and Welding Research Institute, Osaka University, 11-1 Mihogaoka, Ibaraki, Osaka, 567-0047, Japan
[b] Department of Industrial and Manufacturing Engineering, The Pennsylvania State University, University Park, PA, 16802, USA

ARTICLE INFO

Keywords:
Linear friction welding
Numerical modeling
Forging
Pressure-controlled
Plastic flow
Steel
Microstructure
Finite element

ABSTRACT

Linear friction welding is a solid-state joining technology that bonds materials via friction heating and plastic deformation. This process is being extensively researched for welding metallic sheets with different dimensions; however, it involves difficulties in joining thin cross-sections due to extensive misalignment and unsteady plastic extrusion of softened materials at interfaces. This study introduces novel efforts for joining thin cross-sections through pressure-controlled oscillations and displacements, facilitating localized plastic flow essential for high-strength solid-state bond formation. This method is rare, and the results reveal base metal fractures in tensile-tested welded joints of 2 mm thick S45C steel sheets. The interfacial yielding at specific temperatures is obtained by applying pressure corresponding to the temperature-dependent strength of the material. Accordingly, the welding is attempted using a hydraulic-based clamping system designed to accommodate large sheet lengths while allowing precise control of the interface pressure and temperature to facilitate controlled material plastic discharge. However, the requisite joint evolution tracking remains infeasible due to the intricate weld designs and is instead uncovered through novel numerical investigations. Modeling simultaneous oscillations and forging displacement while maintaining pressure depicted the kinetics of continual interfacial deformation. The transient fluctuations in plastic stress and temperature increments distinguish the stages of forging under different conditions. The computed temperature vs. plastic strain and the measured change in interfacial microstructures from martensite to dynamically recrystallized very fine ferrite with fragmented small cementite explain the lower temperature welding for an increase in applied pressure, enhancing the understanding of linear friction welding of thin steel sections for industrial applications.

1. Introduction

Linear friction welding (LFW) technology is in high demand as it can produce strong joints between high-strength lightweight metallic materials [1]. It is widely used in turbine-blisk fabrication in aerospace engines, which requires high tolerance in weld design [2]. It obtains controlled-rate interfacial deformation via high-pressure oscillations and displacements (stroke), yielding solid-state welds in different metals [3]. For example, Tabaie et al. [4] and Yang et al. [5] joined 12-mm-thick Inconel 718-AD730 nickel [4] and GH4169 superalloy [5] sheets using 1.5–3 mm oscillations at 20–35 Hz frequency and 228 MPa pressure, followed by 3 mm axial stroke at 100–340 MPa forging pressures. Further, Zhao et al. [6] welded 20-mm-thick TC11-TC17 titanium alloy sheets, Su et al. [7] joined 12-mm-thick U71Mn high-carbon rail steel, and Liu et al. [8] achieved superior weld strength in 10-mm-thick 9Cr ferrite/martensite steel through LFW. Thus, high-rate shear deformations in LFW effectively induce interfacial yielding and have been a key focus in recent studies. In addition, the strength level of metallic material is expected to increase further in the future, underscoring the necessity for joining the high-strength thin metallic materials. Conventional methods often lead to softening or brittleness in the welded region due to excessive heat input, indicating the need for low-temperature LFW. However, rigorous process control is demanded for thin-sheet LFW.

The foundational research on LFW has focused on the plastic upset of thermally softened materials at the interfaces, coerced to back-and-forth oscillations under high contact pressure [9,10]. The key aspects that are

* Corresponding author.
** Corresponding author.
E-mail addresses: rishabh.shotri@osaka-u.ac.jp (R. Shotri), fujii.hidetoshi.jwri@osaka-u.ac.jp (H. Fujii).

https://doi.org/10.1016/j.ijmachtools.2024.104235
Received 10 June 2024; Received in revised form 6 November 2024; Accepted 27 November 2024
Available online 29 November 2024

Nomenclature

$\mathbf{A_0}$	Oscillation amplitude
C	Stress wave speed
C	Cementite
$\mathbf{C^N}$	Lumped heat capacitance matrix
E	Internal energy
f	Oscillation frequency
F	Ferrite
$\mathbf{F_b}$	Body force
$\mathbf{F_i}$	Internal flux vector
$\mathbf{F^J}$	Internal force vector
h	Material surface conditions
$\mathbf{h_c}$	Convective film coefficient
i	Increment number
k	Thermal conductivity
$\mathbf{k_c}$	Thermal contact conductance
$\mathbf{l_c}$	Characteristic length
L	Lorentz constant
M	Martensite
N	Node
p	Pressure
P	Pearlite
$\mathbf{P_i}$	Applied nodal source vector
$\mathbf{P^J}$	Applied load vector
$\mathbf{q_c}$	Contact heat conduction
$\mathbf{q_{fr}}$	Frictional heat
$\mathbf{q_h}$	Heat loss by surface convections
$\mathbf{q_{pl}}$	Plastic straining-based heat flux per unit volume
$\mathbf{q_s}$	Surface heat flux
$\mathbf{q_v}$	Volumetric heat flux
r	Material resistivity
t	Time
u	Displacement
$\dot{\mathbf{u}}^{\mathbf{N}}$	Nodal velocity
$\ddot{\mathbf{u}}^{\mathbf{N}}$	Nodal acceleration
w	Surface roughness
α	Thermal diffusivity
Δ	Increment
∂	Partial derivative operator
$\dot{\varepsilon}^{pl}$	Plastic strain rate
$\dot{\gamma}$	Slip rate
μ	Friction coefficient
ρ	Material density
σ	Stress
σ_y	Yield strength
τ	Frictional stress
Θθ	Temperature
$\dot{\theta}$	Temperature increment rate
θ^0	Sink temperature
η	Inelastic heat fraction

elucidated include the influence of frictional heating, removal of oxide-film impurities, and consolidation of nascent metallic layers under constant or varying loads on the resulting plastic deformation for solid-state bonding [11–13]. Mukundan et al. [14] reported uncontrolled plasticized extrusion, and Choi et al. [15] observed a 0.2-μm-thick recrystallized region without softening the plasticized area while joining 5- to 6-mm-thick Ti6Al4V alloy at 30 Hz [14,15]. Javidikia et al. [16] and Guo et al. [17] simulated the LFW of 12-mm-thick Ni-based [16] and Ti2AlN-Ti60 titanium [17] alloy under applied pressures of 70–90 MPa and 2–3 mm oscillations at 25–80 Hz and modeled incomplete plastic extrusion at 1158 °C using the DEFORM commercial software. Yang et al. [18] and Yonekura et al. [19] used arbitrary Lagrangian-Eulerian (ALE)-based adaptive remeshing and tracer particles in the ABAQUS software to model the LFW of 12- to 14-mm-thick TB9 titanium alloy [18] and Acryl thermoplastic [19] and reported 1171 °C peak temperature after 5 mm of axial deformation. These developments suggested high-temperature plastic flow across large similar or dissimilar cross-sections. However, commercially important thin-cross-section LFW requires prudent control of interfacial temperature and plastic flow to achieve high-strength welds without uncontrolled extrusion or distortion. Further research on the LFW of thin cross-sections has rarely been conducted, and this study aims to address this gap.

Fig. 1a showcases an automotive frame with various steel sections and their joints [20]. To meet the stringent impact safety standards while simultaneously ensuring light-weight bodies, automotive manufacturers use not only high-strength thin steel sheets but also dissimilar thin cross-section frames (Fig. 1a). In addition, these thin cross-section joints pose dissimilar thicknesses, shifting focus to solid-state LFW joints despite the uncontrolled extrusion and misalignment issues. Owsinski et al. [21], Kelly et al. [22], and Wang et al. [23] attempted the LFW of 100Cr6 alloy steel [21], AISI1020 steel [22], and weathering steels (SPA-H, SMA490AW) [23] sheets with applied pressures, oscillations and forging strokes of 30–350 MPa, 1–3 mm at 15–50 Hz, and 4–12 mm, respectively. However, the minimum thicknesses were restricted to 10–25.4 mm [21–23]. In contrast, this study offers a solution through the development of high-strength joints in 2×50 mm^2 S45C steel cross-sections. The medium-carbon S45C steel, consisting of ferrite and pearlite with an ultimate tensile strength of about 700 MPa, is highly sensitive to the peak temperature in LFW, which can easily change its microstructure from ferrite, pearlite, and bainite to martensite [24–26]. Kuroiwa et al. [24], Gadallah et al. [25], and Aoki et al. [26] successfully achieved an ultimate tensile strength of 766 MPa in 2- to 5-mm-thick S45C steel LFW joints under applied pressures and oscillations of 50–400 MPa and 1–2 mm at 15–50 Hz, respectively. However, these studies primarily focused on elucidating the relationships between microstructures, mechanical properties, and welding parameters instead of providing a comprehensive insight based on a mathematical model into the joint evolution behavior that influences various aspects of the LFW process. This has motivated the ongoing integrated numerical-experimental investigations to reveal real-time weld evolution and transient mechanistic responses that can explore the joining mechanism involved in the LFW of thin steel cross-sections.

The numerically sequential thermal-mechanical coupling in LFW can elucidate the physical phenomena of frictional heat generation and plastic deformation under high-pressure oscillations and axial displacement [27,28]. Baffari et al. [29], Effertz et al. [30], Mcandrew et al. [31], and Jedrasiak et al. [32] utilized two-stage thermo--mechanical calculations with interpolated friction heat and pressure conditions into a single block to examine the local plastic flow during the LFW of Ti6Al4V [29,31,32] and 30CrNiMo8 high-strength steel [30] sheets. These studies revealed a 660 to 1060 °C local temperature gradient for a 40 MPa pressure, 45 Hz frequency, and 6–7.1 mm/s plastic upset rate and primarily modeled the uncontrolled plastic extrusion across the large, unclamped length of the thick cross-sections. Geng et al. [33–35], Okeke et al. [36], and Buffa et al. [37] simulated the precise yielding of 14×10 mm^2 unclamped cross-sections of Ni-based GH4169 [33–35], IN718 [36] and AA6082 [37] alloy sheets, respectively, while modeling consecutive sequences of frictional heating and forging at 50–600 MPa pressures, 2.5–3.3 mm oscillations at 15–30 Hz and 2.7–7.4 mm strokes. However, thin cross-section LFW requires simultaneous heating and upsetting for a subtle plastic flow without any

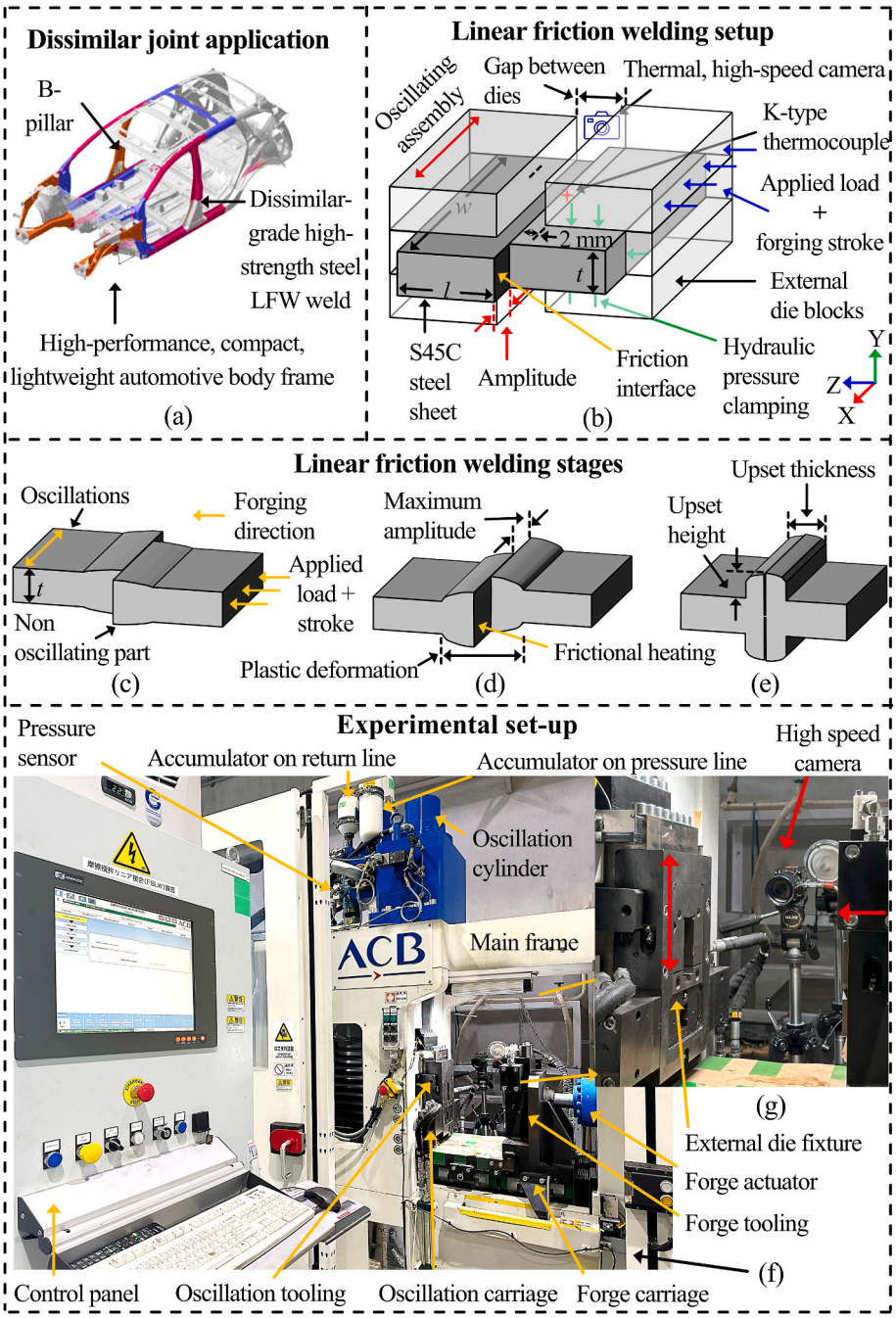

Fig. 1. Overview of linear friction welding setup, mechanism, and joint evolution in thin sheet welding. (a) shows dissimilar joints application [24]. (b) schematic setup for linear friction welding of S45C steel sheets. (c to e) different welding stages. (f to g) experimental setup with enlarged images of external die-fixture arrangement.

misalignment or interfacial distortion of thermally softened interfaces, as investigated in this study.

Furthermore, the LFW of thin-walled workpieces featuring friction surfaces with a high aspect ratio differs from that of regular block-like workpieces with a low aspect ratio. As the aspect ratio of the friction surface increases, the surface becomes more elongated. The vibration direction is typically aligned with the length of the surface, but the reciprocating motion dramatically increases the instability of the welding surface contact. Without the use of special fixtures to constrain the deformation region, it is difficult to achieve a fully bonded, defect-free joint across the entire interface within the effective total shortening stroke. Moreover, prior research on the application of pressure-controlled friction welding of various steels exhibiting complicated phase transformations indicates that increasing the pressure can lower the interface temperature, which significantly affects the microstructure and properties. However, increased pressure also exacerbates vibration instability and compromises alignment precision. Therefore, achieving high-quality, high-precision welding of thin-walled structures within the short duration of the LFW process presents significant challenges.

Thus, this study undertakes a systematic investigation into the LFW of thin cross-section S45C steel sheets via novel numerical and experimental methods. To achieve precise control of local plastic flow without distortion in thin interfaces, a novel fixture assembly with hydraulically operated external die blocks is developed and demonstrated using a real-time monitoring system. The modeling of the high-pressure burn-out phases in the joining of interfaces under varying conditions yields novel

numerical findings. Despite challenges such as extensive mesh distortion and heating, efforts are made to compute the LFW of thin steel sheets accurately using finite element-based methods. Furthermore, the simulation successfully mirrors novel experimental findings, revealing how increased pressure leads to a reduction in welding temperature during the LFW process. These results are crucial for advancing the fundamental aspects of joining metals under controlled welding temperatures, particularly in the LFW of thin metallic sheets. The joint evolution under complex die enclosures and conditions is elucidated, with the key mechanistic responses validated against thermal histories and joint geometries. The mechanical and microstructure characteristics are investigated to understand the process mechanics, with the aim to facilitate the commercialization of thin metallic sheet LFW.

2. Experimental setup of linear friction welding and its joining concept

Fig. 1 illustrates the LFW setup, the welding mechanism, and its application. Fig. 1b depicts the weld geometry, with two sheets positioned between the external dies. Thick metal blocks form external dies for the clamping of thin steel sheets via hydraulic pressure. Fig. 1c, d, and 1e illustrate the three consecutive steps of joint evolution involving simultaneous oscillations and an applied stroke while maintaining the applied load or pressure. Fig. 1f shows the various components of the machine, while Fig. 1g highlights the enlarged external die fixtures and the position of the high-speed camera.

Tooling carriages for forging and oscillations are positioned on the right and left, respectively (Fig. 1f). The hydraulic accumulators for the pressure and return lines, along with a pressure sensor, are positioned at the top of the mainframe. LFW machine is operated through a control panel that includes manual and automatic control options as well as run and emergency stop switches. The panel also features a computer that monitors and records various process conditions in addition to controlling the clamping and unclamping of the external dies. The forge actuators, powered by hydraulic pressure, create the initial contact across the weld cross-section. To initiate welding, an initial pressure of 325 bar is applied to start the oscillation and forging at the specified frequency and load. Fig. 1b illustrates the aforementioned step, showing the simultaneous movement of the external die blocks and the sheet on the oscillating side, as well as the application of the specified load and stroke to the die blocks on the forging side. In the experimental setup (Fig. 1f), the sheets are positioned similarly but with large cross-sectional lengths upright and undergoing vertical oscillations, in contrast to the horizontal sheet orientation depicted in the schematic (Fig. 1b). The initial narrow gap between the external dies, created by 2 mm protruding sheet lengths, enables thermal and high-speed cameras to monitor the upright weld interface for infrared imaging and plastic deformation. Notably, thermal imaging alone cannot clearly capture the interfacial heat generation, as the outward plastic flow often blocks the narrow gap. Therefore, a thermocouple probe is positioned near the interface, attached to the non-oscillating sheet's surface, about 1–1.5 mm from the interface (Fig. 1b). The thermocouple wire is left with sufficient length to accommodate sample movements during welding. Fig. 1c to e illustrate the key stages of welding during the LFW of thin cross-sections. Fig. 1c displays the initial interfacial upset caused by shear and axial plastic deformation. This stage involves conditioning and forging, following the formation of new interfaces under simultaneous high-pressure oscillation and applied stroke (Fig. 1c). The subsequent stages involve burnout and forging, with pressure-controlled plastic flow across the thin cross-sections. This is demonstrated by the increased upset dimensions in Fig. 1d and the final weld geometry in Fig. 1e, following the expulsion of thermally softened interfaces under the applied pressure and stroke, which results in strong metallurgical bonding. These stages mirror the initial, transition, and equilibrium phases of heat and plastic deformation largely predominantly observed in LFW of thick cross-sections [38]. This further highlights that activating the forging alongside oscillations offers efficient control of the weld temperature and interfacial deformation, especially in thin cross-sections. Additionally, Fig. 1e depicts a more protruded and narrow upset, revealing that the interactions between the external die cross-sections and the outward upset ensure intimate contact for bonding. Moreover, Fig. 1c–e does not depict the interfacial plastic flow in the oscillation directions alongside the normal interfacial upset.

3. Theoretical formulation

The theoretical formulation of LFW involves coupled thermo-mechanical analysis to model the heat generated by the oscillatory friction and plastic deformation resulting from the applied pressure and stroke [39]. Fig. 2a shows a schematic of the 3D solution domain, depicting the oscillating and non-oscillating parts interacting under the mechanical boundary conditions. Both parts have a 2 mm length from the interface as a free or unclamped region for thermo-mechanical interactions and plastic deformation. Adjacent to the unclamped (free) region, an external die block, shown on the oscillating sheet in Fig. 2a–is modeled for the controlled plastic extrusion of thin S45C steel sheet cross-sections during LFW. For clarity, similar external blocks on the non-oscillating part are not displayed. The clamped length on the oscillating side is subjected to sinusoidal displacement with an amplitude A and a frequency f in the x direction, with zero displacement in the y and z directions.

The non-oscillating part is subjected to the forging load and stroke at its end face. The remaining faces of the clamped region are assigned

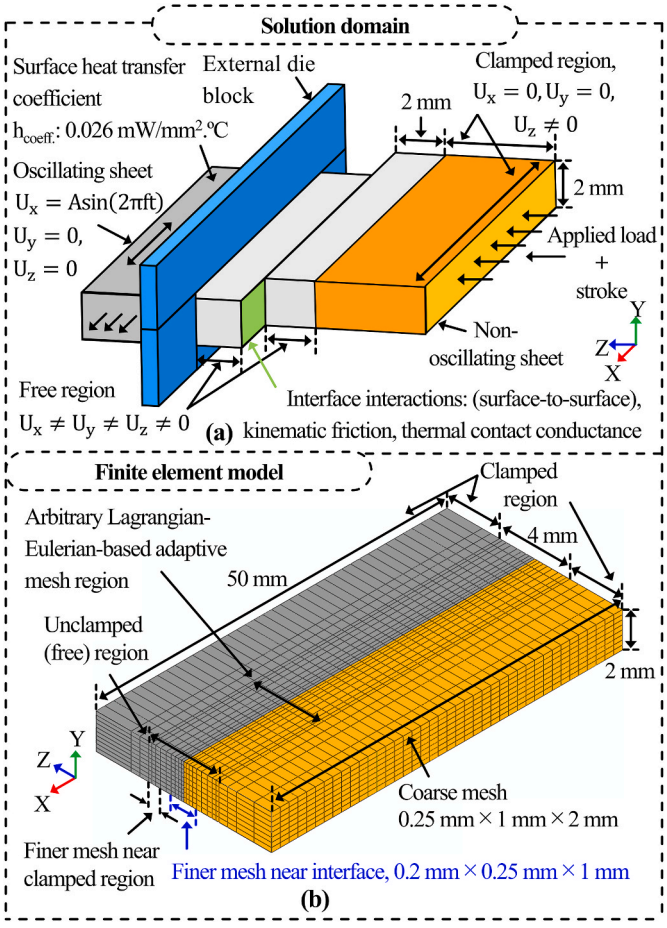

Fig. 2. Numerical modeling of linear friction welding. (a) solution domain with governing conditions across different regions and interface interactions for linear friction welding of 2-mm-thick S45C steel sheets. (b) initial finite element model with arbitrary Lagrangian-Eulerian-based adaptive mesh region.

zero-displacement boundary conditions in the x and y directions while allowing displacement in the z-direction, resulting in plastic deformation of the unclamped region near the interface. The interface interactions are modeled using surface-to-surface kinematic-based contact, incorporating normal pressure contact, master-slave surface heat sharing, a temperature-pressure-slip rate-dependent friction coefficient, and thermal contact conductance [35,40]. Rigid contact is established between the external die and sheet cross-section with a tie constraint. A frictionless surface-to-surface interaction between the external die and the unclamped sheet separates the elements and prevents them from merging during outward plastic deformation. A finite element-based commercial software, ABAQUS (Dassault Systems, ver. 2022), is utilized for modeling the LFW of the thin S45C steel sheets. Fig. 2b shows the three-dimensional finite element model before welding, discretized with 19,210 hexahedral elements. Finer elements with a minimum edge length of 0.2 mm are utilized near the interface and at the end of the unclamped region to capture the significant bending and plastic deformation. The 2 mm sheet thickness is discretized into eight elements, each with a thickness of 0.25 mm. The mesh sensitivity analysis is performed for element sizes of 0.5 to 0.2 mm, with the appropriate accuracy achieved at minimum element sizes of 0.2 mm, 0, 25 mm, and 1 mm in width, thickness, and length directions. An ALE adaptive remeshing strategy is applied in the unclamped region, with a frequency of 40 and 5 sweeps per remeshing cycle (Fig. 2a and b) [33,40,41].

3.1. Thermal-stress analysis

In ABAQUS, an explicit-based, fully coupled thermal stress analysis is conducted to obtain interdependent thermal and mechanical solutions. A three-dimensional solid deformable geometry discretized with C3D8RT elements (8-node thermally coupled brick elements with temperature and displacement degrees of freedom) is used to investigate the thermal softening and interfacial plastic flow during the LFW of thin S45C steel sheets. Additionally, reduced integration and enhanced hourglass control, with a default value of 0.5 balancing viscous and stiffness behavior, help model large plastic deformations without mesh failure, such as extensive element distortion across thin cross-sections [42]. The governing equation for heat generation and transfer is expressed as a combination of the energy balance equation with Fourier's law of heat conduction, given as [41–43],

$$\int_V \rho \dot{E}\delta\theta dV + \int_V \frac{\partial\delta\theta}{\partial x}.\mathbf{k}.\frac{\partial\theta}{\partial x}dV = \int_V \delta\theta q_v dV + \int_S \delta\theta q_s dS \tag{1}$$

where ρ is the material density, k is its thermal conductivity, and E is the internal energy. Term $q_{v,\,s}$ indicate the volumetric and surface heat flux associated with frictional heat generation (q_{fr}), plastic straining-based heat flux per unit volume (q_{pl}), and contact heat conduction across the interface (q_s) [42,43], expressed as

$$q_{fr} = \mu\tau\dot{\gamma} \tag{2}$$

$$q_{pl} = \eta\sigma\dot{\varepsilon}^{pl} \tag{3}$$

$$q_c = k_c(\theta_A - \theta_B) \tag{4}$$

where μ, τ, and $\dot{\gamma}$ (in Eq. (2)) are friction coefficient, frictional stress, and slip rate, which estimate the rate of heat generation by friction work in fully coupled thermal-mechanical interactions. The classic isotropic Coulomb friction is modeled with limiting shear stress conditions (i.e., yield strength/ $\sqrt{3}$ or 200 MPa for S45C steel), incorporating variations in slip rate, contact pressure, and interface temperature. Eq. (5) reflects the Coulomb friction at the S45C steel interfaces before the shear layer formation during LFW [43,44].

$$\mu = ap^b\theta^c\dot{\gamma}^d \tag{5}$$

where a, b, c, and d are obtained as 35.70, −0.601, −0.395, and −0.022 from Ref. [41]. Fig. 3a shows the friction coefficient of the S45C steel interface at temperatures of 0–900 °C and pressures of 50–450 MPa, based on Eq. (5). Notably, Maalekian et al. [44] derived Eq. (5) and the corresponding variable coefficients under pressures of 4–125 MPa, temperatures of 20–2000 °C, and slip rates of 2–3.6 m/s, which slightly differ from the conditions selected in this study. The terms σ and $\dot{\varepsilon}^{pl}$ (in Eq. (3)) indicate the plastic stress and strain rate, respectively, and their cross-product denotes the heat dissipation by plastic deformation in fully coupled thermal-mechanical analysis. η is an inelastic heat fraction that accounts for the inelastic heat dissipation to calculate the temperature rise. It has a default value of 0.9, indicating the maximum energy conversion from plastic deformation [35,36]. The terms A and B in Eq. (4) indicate discrete contact surfaces. k_c represents the thermal contact conductance estimated based on the interface temperature (θ), contact pressure (p), and surface conditions [40,41] as,

$$k_c = 3L\theta wr\left(\frac{\sigma_y}{p}\right)^m \tag{6}$$

where L is Lorentz constant (2.4×10^{-8} $(V/K)^2$), r is material resistivity, and coefficients w and h relate to the surface roughness (0.01 mm) and pretreated material surface conditions (1.5), respectively. σ_y is plastic yield strength (Fig. 4).

The mechanical behavior during LFW is modeled using the equilibrium governing equation expressed as [43],

$$\rho\frac{\partial^2 u_x}{\partial t^2} = \frac{\partial\sigma_{xj}}{\partial_{xj}} + \rho F_x \tag{7}$$

where u and F_x are the displacement and body force in the x direction, and σ is the stress tensor in the xth and jth directions.

3.2. Numerical implementation in ABAQUS

The explicit-based forward-difference time integration of the heat transfer equation reveals the nodal temperature (θ^N) [40–42],

$$\theta^N_{i+1} = \theta^N_i + \Delta t_{i+1}\dot{\theta}^N_i \tag{8}$$

where i, N refers to increment number and node in an explicit dynamic step. Δt is the time increment. The temperature increment rate $\dot{\theta}$ is [40–42]

$$\dot{\theta}^N_i = \left(C^N\right)^{-1}(P_i - F_i) \tag{9}$$

where C^N is the lumped heat capacitance matrix, P_i is the applied nodal source vector, and F_i is the internal flux vector. The mechanical solution is obtained using explicit-based central difference integration [40–42].

$$\dot{u}^N_{i+\frac{1}{2}} = \dot{u}^N_{i-\frac{1}{2}} + \frac{\Delta t_{i+1} + \Delta t_i}{2}\ddot{u}^N_i \tag{10}$$

$$u^N_{i+1} = u^N_i + \Delta t_{i+1}\dot{u}^N_{i+\frac{1}{2}} \tag{11}$$

where u^N, $\dot{u}^N$, $\ddot{u}^N$ are nodal displacement, velocity, and acceleration. The momentum equilibrium equation calculates the acceleration as [40–42],

$$\ddot{u}^N_i = \left(M^{NJ}\right)^{-1}\left(P^J_i - F^J_i\right) \tag{12}$$

where M^{NJ} is the diagonal (lumped) mass matrix. P^J is the applied load vector, and F^J is the internal force vector. The temperature and displacement integrations follow stable time increments, Δt_n [40–42], conforming dilatational (stress) wave interactions within the smallest elements.

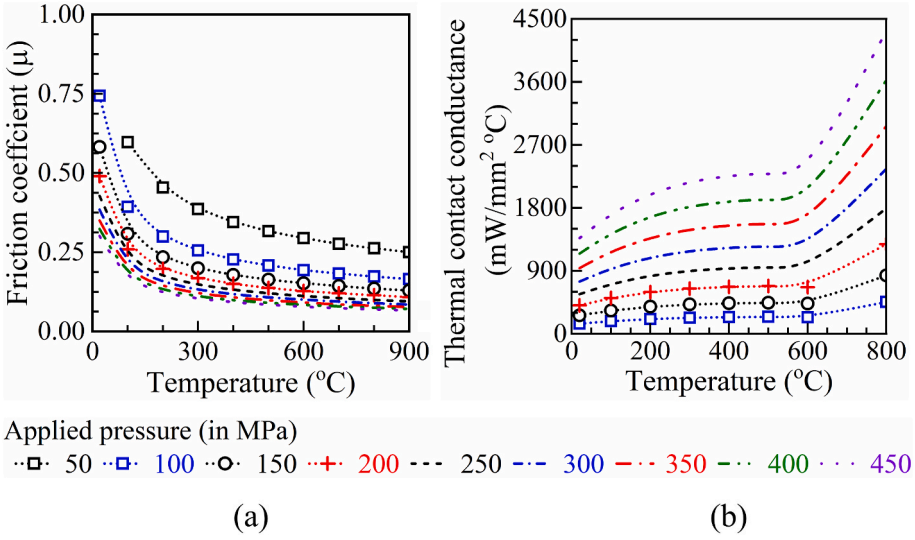

Fig. 3. Interfacial interactions. (a–b) friction coefficient and thermal contact conductance values as a function of different applied pressures and temperatures.

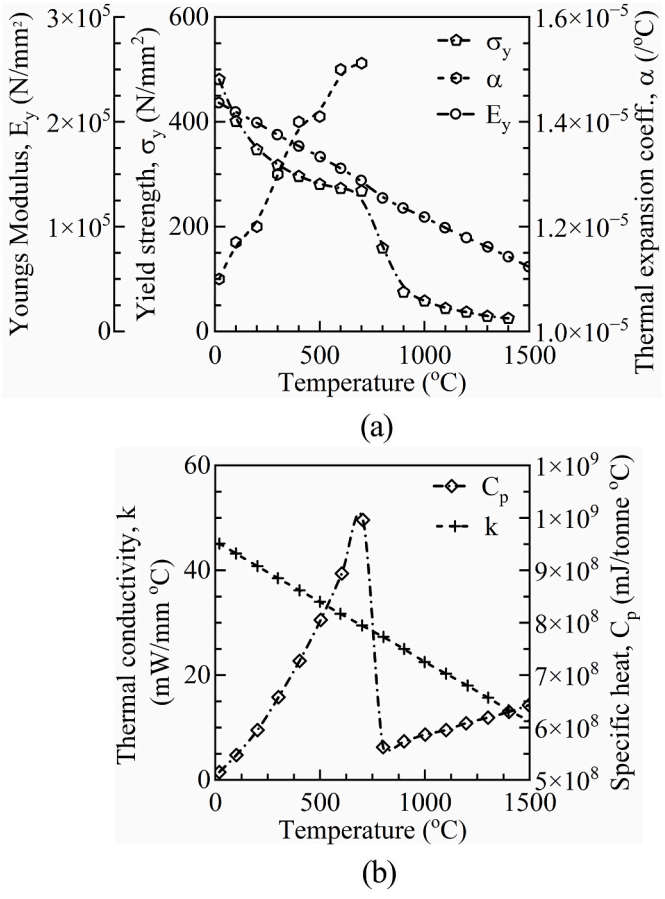

Fig. 4. Material properties. Temperature-dependent properties of S45C steel used in numerical investigations [40]. The material density is 7.8E-09 tonne/mm^3, and the Poisson's ratio is 0.3.

$$\Delta t_n \cong \left(\frac{l_c^2}{2\alpha}, \frac{l_c}{c}\right) \tag{13}$$

where α denotes the material's thermal diffusivity, and c is the stress wave speed across the element with the characteristic length, l_c.

3.3. Assumed boundary conditions and material properties

The initial temperature is predefined as 20 °C. Heat loss by surface convections (Eq. (7)) is established with 0.026 mW/mm^2 °C film coefficient (h_c) [40].

$$q_h = h_c(\theta - \theta^0) \tag{14}$$

θ^0 is sink temperature. Displacement boundary conditions on the clamped regions of oscillating and non-oscillating sheets (Fig. 2a) include [43],

$$u_x = A_0 \sin(2\pi ft), u_y = 0, u_z = 0 \tag{15}$$

$$u_x = 0, u_y = 0, u_z \neq 0 \tag{16}$$

Displacement in the unclamped region is unconstrained. At large strains, the non-linear plastic behavior of S45C steel is defined by its yield point and its post-yield hardening which is represented by the strain rate and temperature-dependent stress-strain values in the ABAQUS plasticity module. Notably, the equivalent plastic stress under the von Mises yield criterion is used to describe the stress state of the material. Fig. 4 shows the temperature-dependent properties of S45C steel used for modeling its thermo-mechanical behavior.

4. Experimental methods

4.1. Materials and experimental procedures

The LFW of S45C steel sheets was conducted by using an ACB LFD15 machine with a 15–150 kN forge force capacity. The oscillation amplitude and frequency range were 0 ± 4 mm and 15–75 Hz, respectively. A maximum upset of 4 mm at a 20 mm/s burn-off rate is feasible [21–23]. The composition of the S45C medium-carbon steel (wt%) included 0.45C, 0.77 Mn, 0.23 Si, 0.08 Cr, and balance Fe [40]. Table 1 shows the specimen details and process conditions. LFW was performed on 2-mm-thick sheets with maximum clamping and a 2 mm protruded length, supporting the selection of a 1–2 mm stroke. A frequency of

Table 1
Presents the details of input conditions, workpiece material, and dimensions.

Parameters	Unit	Values
Applied load/pressure	kN/MPa	20 to 40/200 to 400
Applied stroke	mm	1, 2
Oscillations frequency	Hz	15, 20
Oscillations amplitude	mm	1, 1.5, 2
Sheet material		Steel grade S45C
Sheet dimensions	mm, mm, mm	2, 50, 62 to 63
Thickness, Width, and Length		
Fixture details: material		Die steel
Gap between dies	mm	4, 6

15–20 Hz and an oscillation amplitude of 1–2 mm were chosen to ensure sufficient heat generation while avoiding shear deformation. The cross-sections were cleaned with acetone before being welded. The thermal camera faced the protruded sections of the sheets. A CHINO CPA-T640 infrared camera captured the temperature details at 30 fps [40,41]. A K-type thermocouple wire was spot-welded on the sheet surface 1.5 mm away from the interface. A GL100 Graphtec data logger was used to record the thermal transients in the plasticized regions (within 30–2000 °C) where the thermocouple wire was connected. Rectangular cross-sections across the welded interface were obtained by using an AG360L SODICK (Japan) electrical discharge machine for metallographic examinations. The welded cross-sections and tensile-test fractured surfaces were observed using a Keyence VR 3200 3D optical macroscope [40,41].

4.2. Flow stress measurement

Fig. 5a presents the engineering stress-temperature plot at various strain rates. Fig. 5b presents the corresponding true stress-true strain plots at different temperatures and strain rates. These stress-strain data pertain to the parent S45C steel tested prior to welding. Fig. 5c and d shows the geometrical details of the tensile test specimens. The smaller specimen (Fig. 5d), with a 4 mm gauge length, was used to evaluate the temperature and strain rate-dependent stress-strain behavior of S45C steel [45]. The temperature-dependent stresses of S45C steel (Fig. 5a) validate the applied load/pressure choice, as the peak welding temperature can be controlled by deforming the material at a pressure corresponding to its yield strength [23,40]. For example, the vertical and horizontal lines in Fig. 5a connect the plastic yielding levels of 400, 300, 250, and 200 MPa with their corresponding temperatures of approximately 580, 645, 690, and 735 °C, respectively, at a strain rate of 0.1 s^{-1}. Thus, this approach suggests that LFW at 200 MPa can produce welded structures above the A_1 temperature range, as corroborated by the experimental and numerical results presented here. The plastic yield and temperature ranges may vary slightly with different applied strain rates. However, these results validate the input load conditions of 200–400 MPa (Fig. 5a and Table 1). The true stress-strain data for the parent S45C steel, shown in Fig. 5b, was used to define the plasticity in ABAQUS.

4.3. Mechanical and microstructural characterization methods

The welded cross-sections were polished with waterproof SiC abrasive papers of up to 2000 grits and subsequently diamond polished with 0.9-0.3-0.1 μm particle solutions. A JEOL JSM-7001 FA scanning electron microscope equipped with an electron backscatter diffraction (EBSD) setup was used to observe the microstructures and grain boundary distribution [40,41]. An oxide polishing suspension (non-dry colloidal silica, 0.04 μm, 15–20 min) and a Nital etchant (5 ml HNO_3 + 95 ml ethanol, 30 s) were used to reveal the grain boundary distribution and microstructures of the different welded samples [40]. EBSD results and grain distribution were analyzed using TSL OIM software. A FUTURE-TECH FM-800 micro-hardness diamond tester was used to apply a 100gf load and for a 15 s dwell time to measure the Vickers-based hardness of the welded region.

Fig. 5c and e depict the location and weld geometry of the tensile

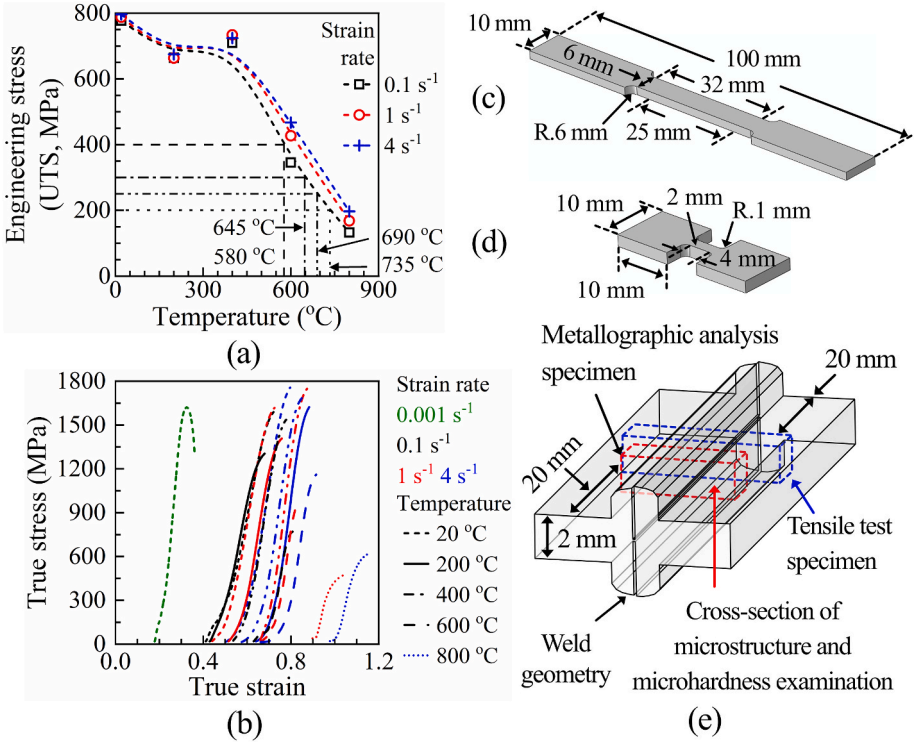

Fig. 5. Stress-strain behavior and temperature dependence of S45C steel. (a) shows engineering stress vs temperature and (b) true stress-strain at different strain rates and temperatures. (c–d) details of tensile test specimens to evaluate (c) weld strength and (d) temperature and strain rate dependent stress-strain behavior of S45C steel. (e) locations and orientations of mechanical and metallographic analysis specimens within the weld geometry.

test. The plasticized upset was polished to create dog bone-shaped flat samples. The paralleled and gauge lengths of the tensile specimens were set as 32 and 25 mm, respectively [46]. The joint strengths were under a 1 mm/min crosshead speed at room temperature using an Instron universal material testing machine.

5. Results and discussion

5.1. Measured input variables

Fig. 6 presents transients of the applied load, oscillations, and stroke during the LFW of the 2-mm-thick S45C steel sheets under different pressure conditions. The 200–400 MPa pressure was applied across a 2 × 50 mm^2 cross-section with a forging load of 20–40 kN. The applied load quickly reached the set value during the initial oscillations. Fig. 6a–d presents the consistent load and oscillations applied with stroke increments of 2 mm. However, the stroke increment rates and process time varied with the applied pressure, i.e., 2.04 to 0.96 s under 200–400 MPa. This is attributed to heat accumulation and plastic-yielding relating to the contact pressure (Fig. 5a and b). Thus, the initial gradual change in the applied stroke with the prolonged high-pressured oscillation under 200 MPa in Fig. 6a denotes insufficient interface heating for plastic deformation. The rapid stroke increments during subsequent stages (Fig. 6a) explain the increasing plastic deformation achieved under high pressure (Fig. 6d). The influence of different pressure-forging characteristics on the weld joint properties and processing temperature is explained in the subsequent sections. A slight arbitrary overshooting in the load amplitudes indicates the experimental recording error (Fig. 6a–d). These forging characteristics were numerically evaluated using the recorded load-oscillation-displacement transients as mechanical boundary conditions.

5.2. Weld joints under different applied pressure

Fig. 7 shows linear friction welded joints obtained under increasing applied pressures. The applied stroke and oscillations were kept constant at 2 mm and 1.5 mm at 20 Hz, respectively. The images (Fig. 7a–d) illustrate normal interfacial upset signifying the weld joints. Fig. 7a' to d' indicate interfacial extrusion in the oscillation directions. Fig. 7a'' and b'' present these bidirectional upset dimensions under applied pressure of 200 and 250 MPa. For 200 MPa, the maximum upset in the normal (black) and oscillation (red) directions were measured to be 1.74 and 1.49 mm, respectively. The corresponding values for 250 MPa (Fig. 7b'') are 1.62 and 1.60 mm, respectively. The upset had similar dimensions due to the constant forging stroke. The slight variation is attributed to the higher applied pressure, which expectedly elevated the interfacial extrusion in the oscillation directions (Fig. 3a). Fig. 7a'' illustrates a 0.25 mm lateral misalignment due to the inadequate pressure. This lateral misalignment was reduced at 250 MPa (Fig. 7b''). Fig. 7a'' and 7b'' present two discrete upset peaks, indicating material ejection from each sheet interface. The upset geometries were arbitrary along the joint length. The respective average values are shown in Fig. 7a'' and 7b''. In contrast, the upset base length remained more uniform (Fig. 7a'' and 7b''), i.e., 2 mm compared with approximately 1.4 mm at the tip. This suggests thinning of the upset under cross-sections of contacting external dies.

Fig. 8 shows the load-elongation curves and tensile test-based fractured specimens obtained under different applied pressures of 200–400 MPa. The oscillation and applied stroke were kept constant at 1.5 mm at 20 Hz and 2 mm, respectively. The maximum tensile load and elongation were measured to be 8.74 kN and 5.69 mm, respectively, for the welded joints obtained under a 250 MPa applied pressure (Fig. 8a). The corresponding joint strength was estimated at 735 MPa. The polished dog-bone-shaped welded specimen fractured across the base material (Fig. 8c). The base metal sample exhibited a maximum tensile load and elongation of 8.34 kN and 9.04 mm, respectively (Fig. 8a and b). The relative tensile strength was determined to be 702 MPa. The maximum tensile load of the joint higher than that of the base material is presumably due to the fact that the very slight, localized work hardening occurred even in the base metal region, approximately 3–5 mm away

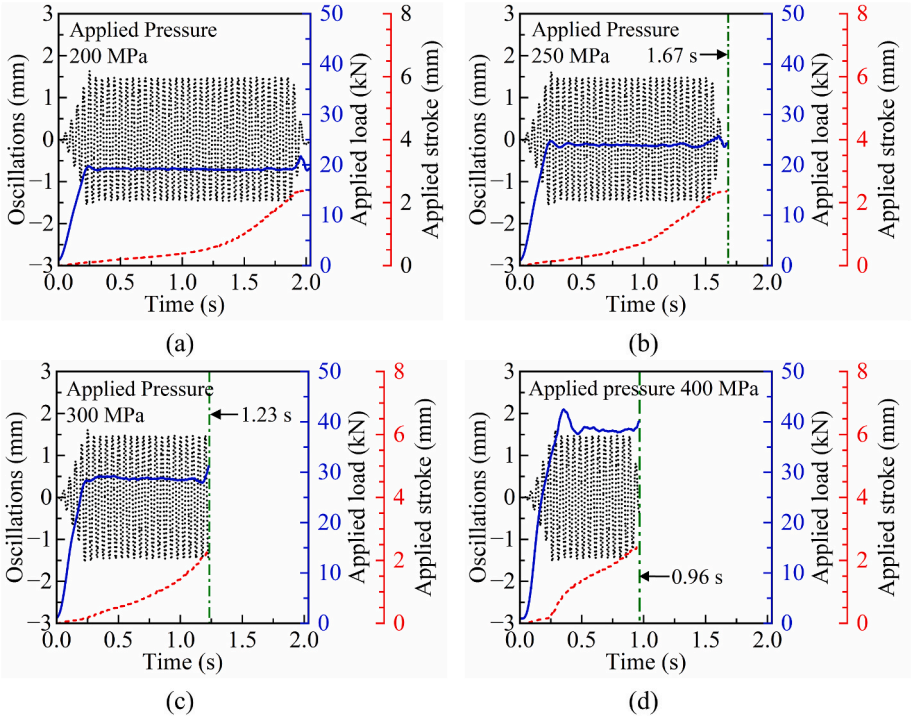

Fig. 6. Load, oscillation, and stroke transients in linear friction welding under varying pressures. (a–d) Time-dependent input variables plots of applied load, stroke, and oscillations under different pressures of (a) 200, (b) 250, (c) 300, and (d) 400 MPa during linear friction welding of 2 mm thick S45C steel. The applied stroke is 2 mm, and the oscillation is 1.5 mm at 20 Hz.

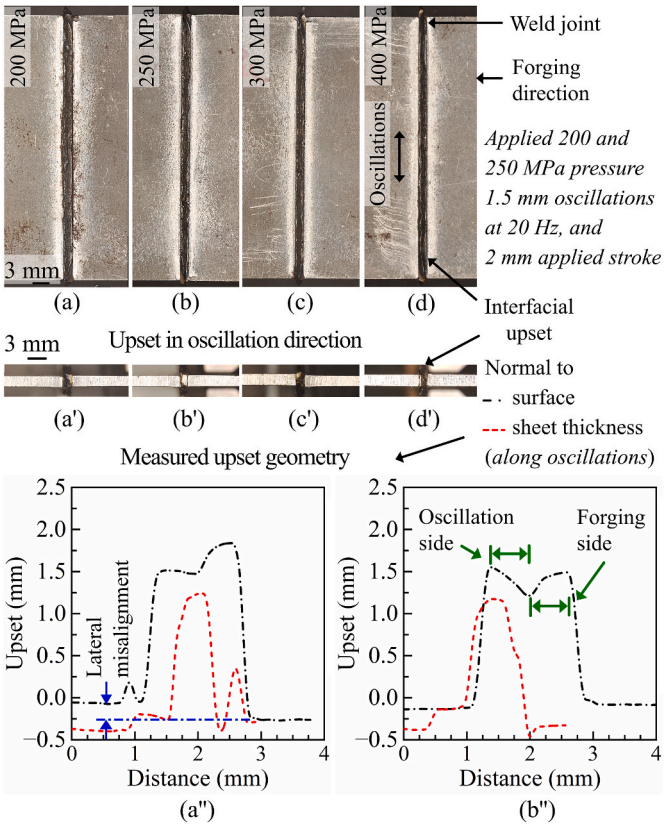

Fig. 7. Influence of applied pressure on normal interfacial upset. (a to d) shows the top surfaces of welded specimens obtained under applied pressures of (a) 200, (b) 250, (c) 300, and (d) 400 MPa. (a' to d') shows the corresponding joint cross-sections. (a'' and b'') provide measured geometry dimensions of interfacial upset in the normal and oscillation directions under (a'') 200 and (b'') 250 MPa applied pressure. The frequency, amplitude, and applied stroke are 20 Hz, 1.5, and 2 mm, respectively.

from the welding line of the joint because high pressure is applied during fabrication. Fig. 8a–c reveal a smaller elongation and greater weld strength, indicating interface hardening during LFW, explained in subsequent sections. A maximum tensile load and joint strength of 8.89 kN and 748 MPa were achieved under an applied pressure of 250 MPa. The maximum elongation was limited to 5.33 mm. Further, the ductile base metal fractured farthest from the joint interface under the 250 MPa applied pressure. The weld joints obtained under 300 and 400 MPa pressures exhibited maximum loads (strengths) of 8.58 kN (722 MPa) and 8.15 kN (686 MPa), respectively. The elongations before ductile failure away from the welded interface were 5.69 and 5.57 mm, respectively. Clear remnants of carbon fibers snapped along the tensile direction can be seen, demonstrating ductile fracture characteristics and indicating a robust interfacial bond strength [47]. These results indicate adequate heat generation and plastic deformation under the specified conditions.

5.3. Microstructure development under different pressures in LFW

Fig. 9 shows the S45C steel base and welded microstructures under different applied pressures. Fig. 9a shows the variations in microstructure distribution due to interfacial plastic deformation. The base metal microstructures consist of ferrite and pearlite (Fig. 9b). Fig. 9c–f depict differential weld conditions with interfacial microstructures under 200, 250, 300, and 400 MPa pressure. At 400 MPa, the welded region contains dark grey, extremely fine ferrite (~0.5 μm) formed by dynamic recrystallization and very small cementite particles (~0.1 μm) with a white contrast by the fragmentation of lamellar cementite in pearlite. These microstructures indicate that LFW is conducted below the A_1 temperature for an applied pressure of 400 MPa. For an applied pressure of 200 MPa, the microstructures are presumably formed between the A_1 and A_3 (inter-critical) temperature range with alpha + gamma followed by martensitic transformation of gamma during rapid cooling after LFW. The results are presented at a higher magnification in the upper right quadrant (Fig. 9b–f). The volume fraction of martensite decreased at higher pressures because interface temperature becomes lower (Fig. 9f). The microstructure under a 250 MPa applied pressure is similar to that under 200 MPa, consisting of ferrite and martensite, but with a finer microstructure and lower martensite fractions. The welding temperature was likely within the inter-critical temperature range but slightly lower than that at 200 MPa applied pressure. At 300 MPa, some fine cementite particles that are more adamant at higher pressure exist with extremely fine ferrite and a smaller fraction of martensite. This indicates that the welding temperature was just above the A_1 point. Thus, the interface microstructures observed at different applied pressures speculate peak welding temperatures. Kuroiwa et al. [21] reported similar microstructures and temperature ranges above and below the A_1 point under

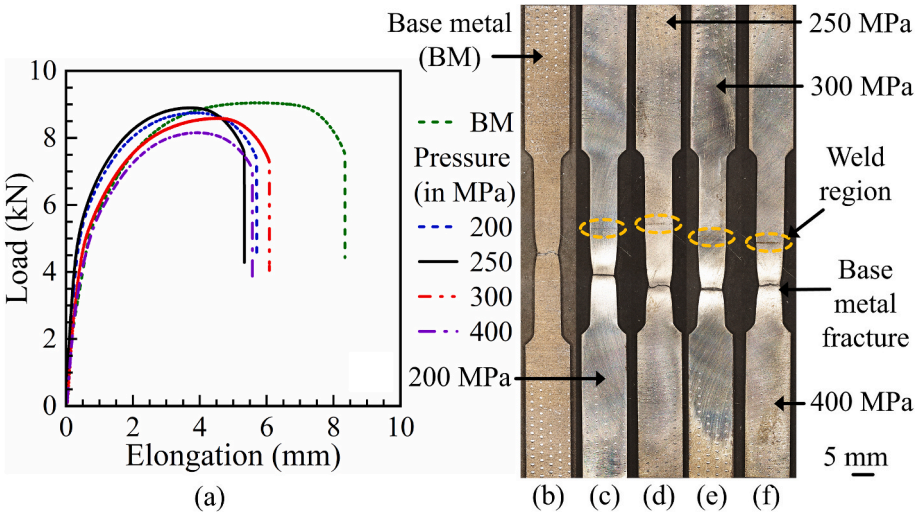

Fig. 8. Load-elongation and fracture of linear friction welded joints under varying applied pressures. (a) load vs elongation plot of base metal and welded specimen obtained under applied pressures of 200, 250, 300, and 400 MPa. (b to f) denote the corresponding fractured specimens. The oscillations and applied stroke conditions include 1.5 mm at 20 Hz and 2 mm, respectively.

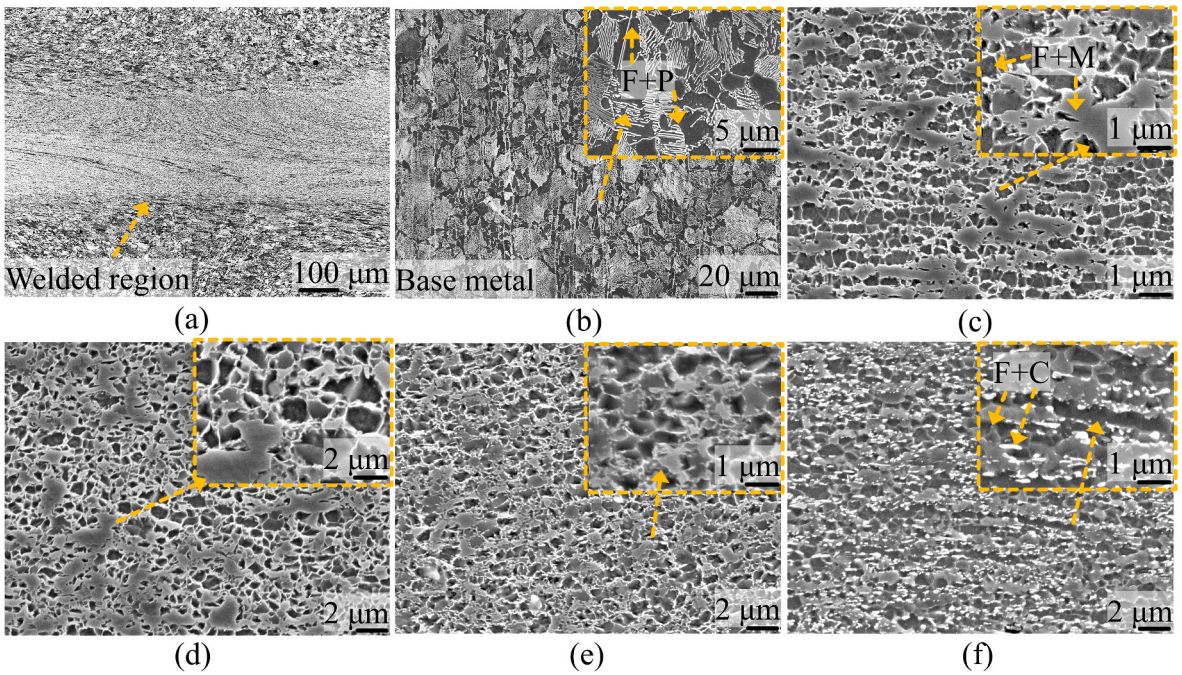

Fig. 9. Microstructural evolution in S45C steel linear friction welded joints under varying pressures. (a) Microstructure distribution of LFW joint at 250 MPa applied pressure. (b) base metal microstructures. (c to f) microstructures of weld joints at (c) 200, (d) 250, (c) 300, and (d) 400 MPa applied pressure. The applied forging stroke is 2 mm. C, F, M, and P refer to cementite, ferrite, martensite, and pearlite, respectively.

applied pressure of 200–400 MPa and explained the change in the microstructures with distance from the weld center, as established in Fig. 10.

Fig. 10 illustrates the development of the linear friction welded microstructures under a similar 2 mm forging stroke. Fig. 10a, d, 10g, and 10j present the welded regions formed under 200, 250, 300, and 400 MPa applied pressures and depict grains distribution of similar average diameters ranging from 0.61 to 0.75 μm with standard deviations in the range of 0.24–0.50 μm. The dissimilarity in their formation mechanisms is revealed from their orientations (color). In the welded regions obtained under applied pressures of 200 MPa and 400 MPa (Fig. 10a and j), the <111> (blue)//OD (oscillation direction) orientation, which is associated with shear deformation accompanying oscillation, is dominant, although the 200 MPa weld has a greater fraction of other orientations due to phase transformation. The grain morphologies under different applied pressures become increasingly dissimilar further away from the welded region. The average grain sizes in the regions composed of deformed and partially recrystallized grains 0.25 mm and 0.5 mm from the center in the 200 MPa joint were 5.57 and 8.24 μm, respectively (Fig. 10a–c). The corresponding values for the welded joints obtained under 400 MPa pressure were 2.44 and 4.94 μm, respectively. This signifies that the microstructures in regions distant from the weld center under high applied pressures comprise elongated grains without refinement, reflecting a narrow heat-affected area and largely plasticized welded regions.

Fig. 10b, c, and 10f illustrate larger grains under applied pressure of 200 and 250 MPa, which is attributed to a greater heat-affected area and a smaller plastic deformation region. The average grain sizes in the regions 0.25 mm and 0.50 mm from the center in the 250 MPa joint were 1.41 and 7.03 μm, respectively (Fig. 10d–f), while those in the 300 MPa joint were 1.14 and 2.76 μm, respectively (Fig. 10g–i).

Overall, Fig. 10 illustrates the distribution of plastic deformation and temperature in linear friction welded joints obtained at different applied pressures. For instance, Fig. 9c shows that at 200 MPa, the peak temperature was above the A_1 point, and the presence of extremely fine equiaxed ferrite grains (Fig. 10a) suggests significant plastic deformation at high temperatures. At 0.25 mm from the weld center, grain refinement was limited (Fig. 10b), and the equiaxed features suggest the influence of phase transformation and relatively small plastic deformation. At a 0.5 mm distance (Fig. 10c), the temperature was further lower, with less plastic deformation, and the microstructures lacked refinement or severe deformation of grains. At 250 MPa, plastic deformation becomes dominant at high temperatures, with dynamic recrystallized grains observed over a wider area (Fig. 10d to e). A similar trend was observed at 300 MPa (Fig. 10g to h). The microstructures in Fig. 10f (250 MPa) and Fig. 10c (200 MPa) are similar as well. Fig. 10f depicts a lower temperature and less plastic deformation at a 0.5 mm distance. Conversely, the partial refinement due to recrystallization and the significantly deformed grains at 0.5 mm from the weld center and for the 300 MPa joint (Fig. 10i) indicate large plastic deformation at relatively low temperatures. At 400 MPa, the lowest temperature was observed (Fig. 9f), and the partial refinement due to recrystallization and elongation at and away from the weld center, respectively, indicates low-temperature plastic deformation (Fig. 10j and k). Therefore, dynamic recrystallization may also occur below the A_1 point. Figs. 10h and k depict the microstructures after plastic deformation at a higher temperature in the former 300 MPa joint than in the latter 400 MPa joint. The results in Figs. 10k and i appear similar, suggesting a reduction in the frictional heat area with an increase in pressure. However, the microstructures in Fig. 10l, i.e., 0.5 mm away from the weld center, fairly show plastic deformation at reasonable temperatures, explaining the consistent distribution of heat and the temperature reduction trend with an increase in applied pressure.

5.4. Computed joint evolutions as a function of mechanical responses

Fig. 11 illustrates joint evolution during LFW with a computed distribution of temperature at different instants. The oscillating sheet was sectioned at the center to examine the progress of joint formation. Fig. 11a shows the interfacial heating due to friction from the high-pressure contact oscillation. The peak temperature reached 198 °C at 0.65 s. Fig. 11b shows the onset of interfacial plastic deformation with a maximum interface temperature of 370 °C at 1.18 s. Fig. 11c shows the growing interfacial plastic deformation with a maximum temperature of

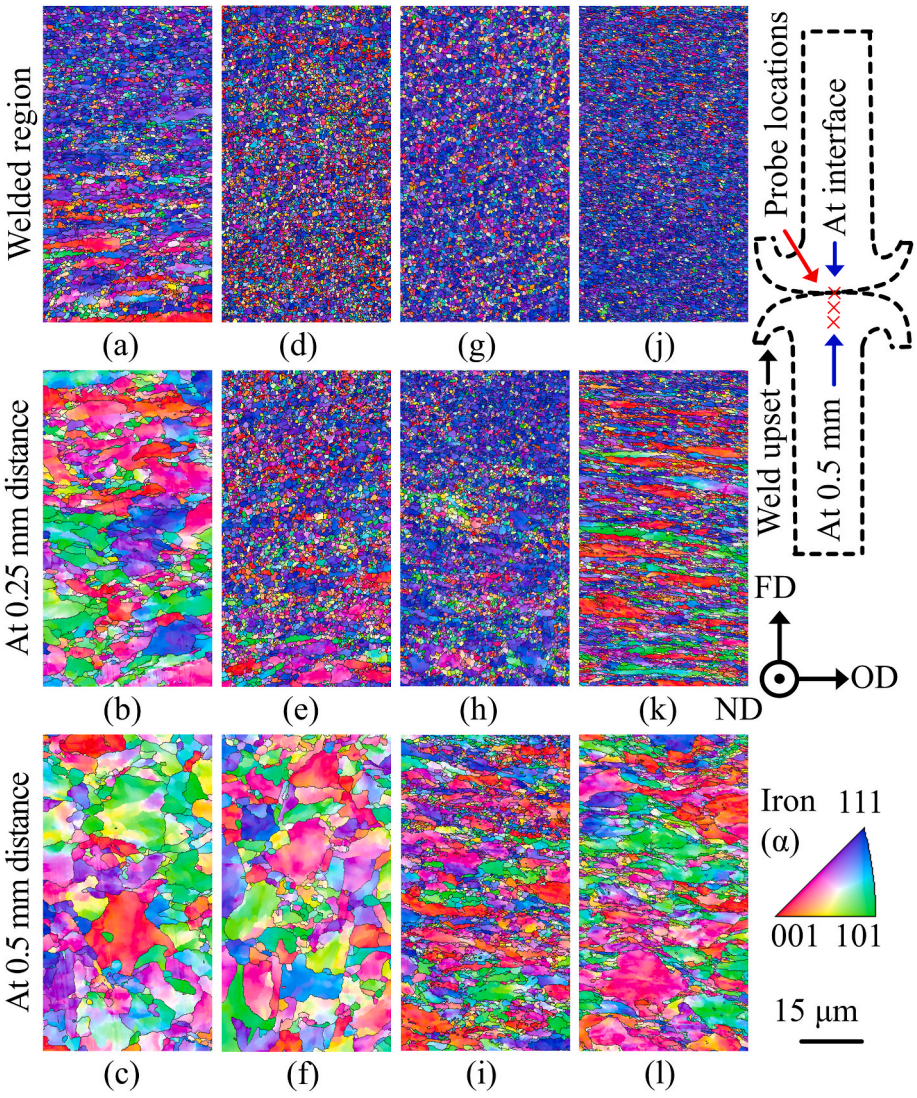

Fig. 10. Microstructure and grain evolution in linear friction welded joints at varying pressures. (a to c) show inverse pole figure maps at (a) weld interface and at a distance of (b) 0.25 and (c) 0.5 mm (a, d, g, and j) shows inverse pole figure maps obtained under (a) 200, (d) 250, (g) 300 and (j) 400 MPa applied pressure. The corresponding variations at variable distances are presented in (e and f) 250, (h and i) 300, and (k and l) 400 MPa applied pressure. The black lines draw grain boundaries with misorientation of 15° or higher. The crystal orientation parallel to OD is displayed as a color corresponding to the standard triangle. The step size is 0.12 μm. The schematic on the right indicates the probe locations (at the interface and 0.25 and 0.5 mm distance) where the microstructures have been taken. (For interpretation of the references to color in this figure legend, the reader is referred to the Web version of this article.)

540 °C at 1.67 s. The computed results show interfacial extrusion in both the oscillation direction and the direction normal to the sheet surface. The maximum interface temperature was computed to be 710 °C at 1.87 s. The maximum temperature exhibited an elliptical distribution across the plastically deforming interfaces. This denotes a lack of friction heat in the upset-out material under inadequate forging contact (Fig. 11d). In subsequent instants, the heat conduction and frictional heating were aided by the forging contact of the external die cross-section (Figs. 1 and 11e). This resulted in a homogeneous temperature distribution and plastic deformation of the interfacial upset at later stages (2.04 s). A supplementary video (Vs1) in AVI format is attached, demonstrating the simulation of linear friction welding and the evolution of nodal temperature distribution across the welded cross-section.

Fig. 12 illustrates the distribution of equivalent plastic strain in the computed LFW cross-section. Fig. 12a depicts the onset of plastic deformation under an initial interfacial plastic strain of 0.7 at 1.26 s. At 1.63 and 1.79 s, the interfacial upset increased under the maximum plastic strains of 1.0 and 1.3 (Fig. 12b and c). The maximum computed strain at the center is related to the joint evolution due to outward plastic flow and oxide film removal. Fig. 12d shows that the maximum plastic strain was 1.7 at 2.04 s across the computed interface. The slight irregularity in the strain distribution is attributed to the trivial variations in compression and shear deformation at the welded interface. In addition, the discrete maximum strain spots over the outer surface of the interfacial upset were induced by the pressure impulses applied by the external dies cross-sections at later stages.

Fig. 13 demonstrates the distribution of equivalent plastic stress and displacement in the Y-direction, which is referred to as normal plastic deformation. The two sets of results are presented to explain the state of joint evolution during LFW. Fig. 13a shows the initial contact and oscillation at 0.04 s under an applied pressure of 200 MPa. The plastic stress at this stage remained uniform, with a maximum magnitude of 700 MPa. The concurrent mechanical compression and shear produced this stress at the contacting interface. Fig. 13b indicates the onset of plastic yielding at 1.55 s under the maximum plastic stress of about 1050 MPa. At 1.67 s, the interfacial stress (Fig. 13c) reached 1750 MPa with an elliptical distribution. At this stage, the plastic stress gradient distribution was related to inadequate compression shearing across the

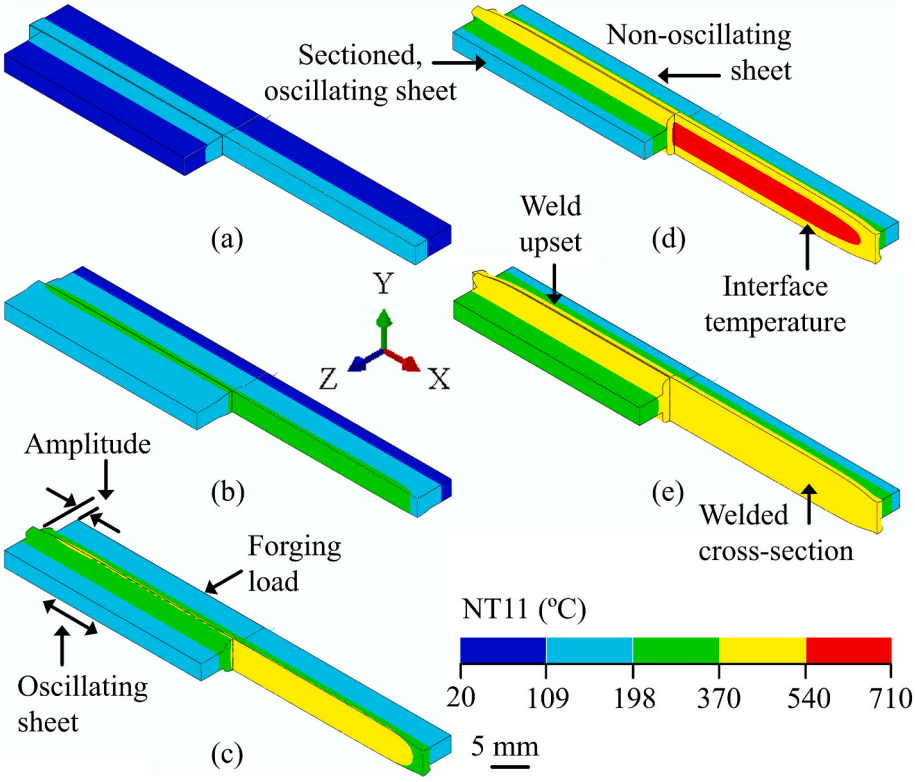

Fig. 11. Evolution and thermal results. Computed weld evolution as a function of nodal temperature distribution at 200 MPa applied pressure. The sectioned portion of the oscillating sheets contemplates high-temperature interfacial plastic deformation at different time instants of (a) 0.65, (b) 1.18, (c) 1.67, (d) 1.87, and (e) 2.04 s. The oscillations and applied stroke are kept at 1.5 mm at 20 Hz and 2 mm, respectively.

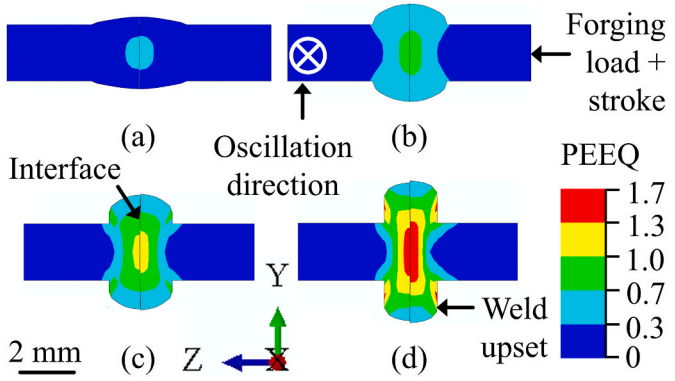

Fig. 12. Time-dependent strain in joint cross-section. Figure shows the computed progress of joint formation as a function of equivalent plastic strain (PEEQ). (a to d) shows equivalent plastic strain at different time instants of (a) 1.26, (b) 1.63, (c) 1.79, and (d) 2.04 s. Other conditions include 200 MPa applied pressure, 1.5 mm oscillations at 20 Hz, and 2 mm applied stroke.

initial interfacial upset. Fig. 13d indicates the final weld geometry at 2.04 s, with a more uniform stress distribution across the interfacial upset. The external die cross-section interactions further plasticized the upset with the high-stress contours indicated over the outer surface (Fig. 13d). The interfacial upsets (U2) in Fig. 13e–h depict a bi-directional plastic flow, which corroborates the sliced cross-sections in the green contours shown in Fig. 13e along with initial weld geometry. Figs. 13f and g illustrate the progress of plastic deformation with a maximum interfacial upset of 0.3–1.5 mm between 1.35 and 1.76 s. This is attributed to the continued high-pressured oscillation and forging stroke. The weld joint at 2.04 s in Fig. 13h explains the maximally constrained interfacial upset for intimate contact and metallurgical bonding under the applied pressure of 200 MPa.

5.5. Temperature, upset, plastic stress-strain transients

Fig. 14 shows the calculated interfacial maximum temperature, equivalent plastic stress, and strain during joint formation under different applied pressures. The normal upset was calculated based on the plastic deformation of the interface ends. Fig. 14a shows the nodal temperature history of the LFW joints obtained under applied pressures of 200–400 MPa. The temperature, stress, and strain were probed at the interface center, indicated by the red mark in the meshed geometry on the right. The temperature increment rate differentiates the initial and final forging stages at the 200 MPa applied pressure due to the gradual increase in stroke (Fig. 6a). A maximum temperature of 696 °C was calculated at 1.92 s. This implies that the interface temperature continues rising during forging with oscillations until the peak value is reached, which is governed by the applied pressure. The calculated peak temperature was slightly short of the expected A_1 temperature (as indicated by the welded microstructures in Fig. 9c). This is due to a slight inaccuracy associated with the pressure-temperature-dependent conditions of coefficient of friction and thermal contact conductance. The peak temperatures calculated under other conditions follow this deviation as well. The maximum temperatures were calculated to be 659, 631, and 614 °C under the applied pressure of 250, 300, and 400 MPa, respectively. The reduction in maximum computed temperature with increasing applied pressure aligns with the temperature-dependent yielding of S45C steel (Figs. 4 and 9d-f). The temperature increment rate was more uniform under a large load intensity (400 MPa, pressure), causing an expedited rise in applied stroke or vice versa.

Fig. 14b shows the normal interfacial upset calculated at the end of a cross-section (i.e., at the red mark at the interface end). The maximum upsets were 1.48, 1.44, 1.39, and 1.36 mm under the applied pressure of 200–400 MPa. The nearly consistent interfacial upset indicates

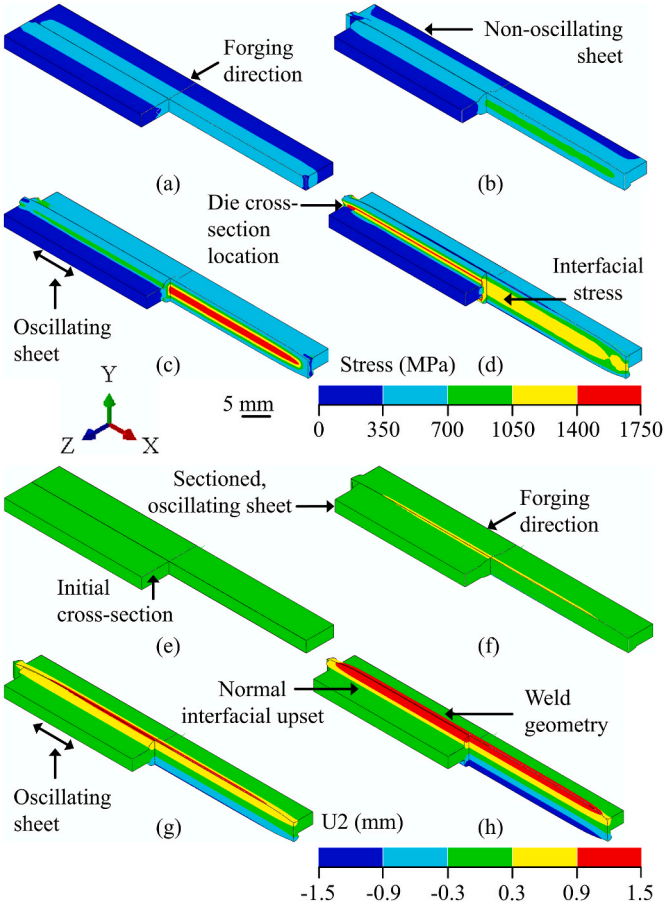

Fig. 13. Stress and displacement in linear friction welding of S45C steel sheet. The figure shows the computed progress of (a to d) equivalent plastic stress distribution and (e to f) normal interfacial upset at time instants of (a and e) 0.04, (b and f) 1.55, (c and g) 1.67, and (d and h) 2.04 s. Oscillations and strokes are 1.5 mm at 20 Hz and 2 mm.

equivalent plastic deformation for an applied 2 mm forge stroke. The oscillation amplitude was kept constant at 1.5 mm. The slight variations in upset at higher pressures denote lower-temperature plastic deformation conditions (Fig. 14a). These variations are also visible in the measured normal upsets of 1.74, 1.62, 1.58, and 1.54 mm for the LFW joints obtained at 200–400 MPa pressure (Fig. 7). Moreover, the measured and calculated normal interfacial upsets are similar, and the observed variations are due to the slightly unsymmetrical, wavy plastic flow with arbitrary edge thinning during LFW, unlike the symmetrical plastic flow observed from the computational investigations.

Fig. 14c depicts the fluctuations in interfacial equivalent plastic stress due to the concurrent actions of oscillations and plastic deformation under various applied pressures. The plastic stress variations follow the differential rates of temperature increment under different pressures. At the 200 MPa applied pressure, the plastic stress fluctuated between 100 and 600 MPa for the initial 1.6 s of the applied forging stroke and oscillations. For the final 0.4 s, it subsequently fluctuated between 400 and 1600 MPa. The surge in stress fluctuations at the 400 MPa applied pressure denotes expedited increments in interfacial plastic flow under large loads. The increased rate of forging strokes corroborates this. The shorter time for material ejection under relatively lower temperatures under large loads reasonably promoted smaller upset heights and large upset thicknesses (Fig. 1) under a constant stroke and plastic deformation volume. The computed amplitudes of maximum stresses were similar, representing the threshold flow stress values for plastic yielding of the thermally softened interfaces (Fig. 5a, b, and 14c). For the intermediate 250 and 300 MPa applied pressures, the stress fluctuations were more contained over subsequent increments, which implies suitable oscillation forging conditions for interfacial yielding.

Fig. 14d illustrates the relationship between the distributions of peak temperatures and equivalent plastic strain at various distances from the weld interfaces. The peak values of plastic strain were estimated to be 1.66, 1.67, 1.59, and 1.47 under the applied pressures of 200, 250, 300, and 400 MPa. For a similar stroke, the differential plastic strain corresponds to the influence of the peak temperature, which is governed by the applied pressure at the weld center. At lower applied pressures, the temperature-plastic strain scatter plots located in the upper right area exhibit a steeper slope. This indicates a concentration of plastic strain and temperature at the weld interface. Similar results are observed based on the distributions of grain morphologies in Fig. 10. At higher applied pressures, the scatter plots in blue and green, i.e., at 300 and 400 MPa, have a gradual slope, explaining the low temperature and its gradient illustrated in Fig. 10g to l. The calculated maximum temperatures and plastic strains were slightly higher due to the small processing time under a large load, i.e., 400 MPa. Fig. 10l closely supports these results.

5.6. Real-time weld monitoring

Fig. 15 shows the progress of joint formation based on the recorded temperature and plastic deformation during the LFW of the 2 mm S45C steel sheets. Fig. 15a–e shows infrared-based thermal images captured at different time intervals. The thermal imaging results (Fig. 15a–e) were calibrated considering a 0.85 emissivity to account for oxidation and deformation effects [40]. Fig. 15a' to e' show plasticized welded surfaces recorded by the high-speed camera. Fig. 15a' shows two sheets inside the outer die cross-section. The die-sheet oscillating assembly is on the left, while the forging load and displacement are applied on the right die cross-section. Each sheet protrudes 2 mm from the die, as shown by the blue dashed rectangle (Fig. 15a'). The external dies are indicated by the yellow dashed lines in Fig. 15b' and 15e'. Fig. 15a shows the interface heating and a maximum temperature of 155 °C during oscillations at 0.2 s. The corresponding stroke was 0.18 mm, ensuring a high-pressure mechanical contact (Fig. 15a').

At 0.7 s, the temperature increases to 197 °C across the cross-section, with the corresponding stroke being 0.45 mm (Fig. 15b). Fig. 15b' shows the initial material upset (grey waves) at the center of the protruded lengths. At 1.9 s, the interfacial upset grew under a 0.68 mm stroke (Fig. 15c'), with the maximum temperature being 292 °C (Fig. 15c). At 2.7 and 3.9 s, the heat generated was transmitted across the welded area, with the maximum temperature being 467 and 560 °C, respectively (Fig. 15d and e). Fig. 15d' and 15e′ show homogeneous weld upsets under forging strokes of 0.84 and 1.09 mm. A supplementary video (Vs2) in AVI format demonstrates these high-speed recorded results (Fig. 15a'–e').

Figs. 15f and g compare the computed and measured temperature transients for LFW under different pressures. Notably, the microstructures presented in the previous sections clearly explain the welding temperature range around the A_1 point, i.e., approximately 700 °C. In contrast, the lower temperature ranges presented in Fig. 15 are attributed to the deviations in probing positions away from the interface owing to outward plastic deformation. Fig. 15f shows the thermocouple readings with a peak of 517 °C at the 200 MPa applied pressure. At the 250 MPa applied pressure, a peak of 495 °C was achieved. The peak temperature dropped with an increase in applied pressures during LFW, which aligns with the microstructure details. The welding temperature conditions were met due to the material's temperature dependence. The computed results reasonably conform to these weld conditions. Lower peak temperatures of 412 and 402 °C at higher applied pressures of 300 and 400 MPa corroborate this observation. A slight variation in the thermocouple wire position (1.4–1.6 mm from the interface) is presumed to have led to a similar temperature range. Further, the similar estimated temperatures at higher pressures (denoted by the small circles

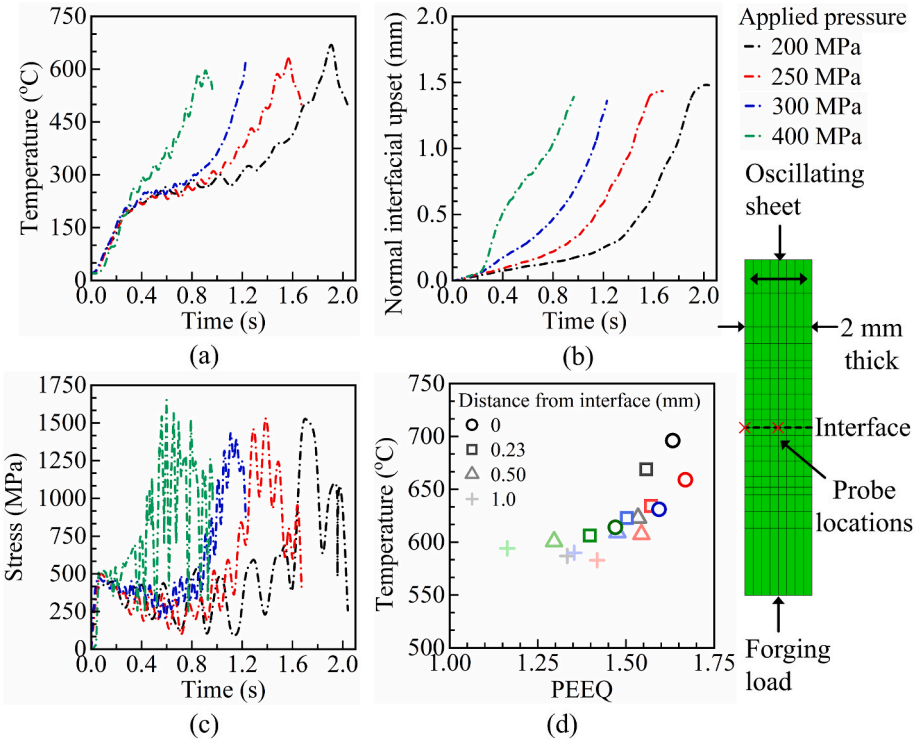

Fig. 14. Effect of applied pressure on thermo-mechanical responses. Figures show computed transients of maximum (a) interface temperature, (b) normal interfacial upset, (c) equivalent plastic stress, and (d) temperature vs. equivalent plastic strain (PEEQ) at different distances from the interface for different applied pressure conditions. The applied oscillations and strokes are 1.5 mm at 20 Hz and 2 mm, respectively.

(in Fig. 15f) highlight the slight limitations in the friction and contact conductance conditions (Fig. 3a and b). Fig. 15g presents the computed and measured transients of the interface temperature (recorded using the infrared thermal camera), which reasonably fall short of the welding temperature generated by progressive upsetting and heat dissipation across the welded interface.

5.7. Plastic deformation kinetics

Fig. 16 illustrates the interfacial deformation kinetics during the joint evolution through velocity vectors corresponding to oscillations and displacement under forging load. The sectioned cross-sections present the velocity vectors at three different stages. First, with the oscillating sheet at the maximum amplitude position with respect to the sheet under forging load (Fig. 16a). The time instance is 0.31 s, with velocity vectors mark the maximum acceleration. The computed stage at 0.34 s represents the maximum inward acceleration (Fig. 16b).

Fig. 16c denotes the intermediate position of the oscillating sheet at 0.43 s, where the normal velocity vectors across the weld interface illustrate the axial compression under the high-pressure forging stroke. The upsetting rate at this stage is equivalent to the displacements (blue-cyan vectors) at about 10 mm/s. The slightly smaller plastic deformation in Fig. 16a–c indicates the initial welding stages at 0.31–0.43 s from a total of 1.67 s (Fig. 6b) of simultaneous oscillations and plastic deformation-based forging. This upsetting continued until the 2 mm forging stroke was achieved. The applied pressure was kept at 250 MPa, and the friction heating from oscillations intermittently raised the weld interface temperature. The intricacy of the concurrent oscillations and forging grew as the plastic deformation and weld upset progressed, as explained subsequently.

5.8. Variable process conditions and role of external die setups

Table 2 provides the processing details of LFW of 2 mm thin sheets when the applied frequency, amplitude, and stroke are discreetly varied.

Fig. 17 shows the linear friction welded cross-sections computed for three different weld geometries. Fig. 17a, d, and 17g, respectively, display the nodal temperature, equivalent plastic strain, and interfacial upset for the welded assembly with a 4 mm initial gap between the external dies. Fig. 17b, e, and 17h and Fig. 17c, f, and 17i show the corresponding results for the weld geometries without an external die and with a 6 mm gap between the external dies. The boundary conditions for the sheets were relevant until the die covered their surfaces (in Fig. 17a and c). For sheets lacking an external die, the area within 2 mm of the weld interface remained unconstrained (Fig. 17b). Fig. 17a, b, and 17c explain that the unconstrained interfacial upset (Fig. 17b) resulted in a homogeneous distribution of the maximum temperature range across the weld cross-section. This is due to the heat accumulation in the absence of heat conduction by the external die cross-section. Figs. 17a and g shows the inward bend of the interfacial upset under the pressure applied by the external die cross-section for intimate mechanical contact and metallurgical bonding (Fig. 9). This explains the concentrated and uniform plastic strain distribution across the weld cross-section (Fig. 17d). Figs. 17c and f displays the dissipated nodal temperature and plastic strain distribution across the interfacial upset. For the larger 3 mm protruded sections, the smaller plastic strain denotes that the 2 mm forging stroke was inadequate. A small interfacial interaction was observed at the maximum temperature during large-area plastic deformation. The external dies exhibited minimal interaction with the interfacial upset for plastic flow and heat dissipation.

Fig. 18 presents the LFW joints, their cross-sections, and their upset geometry details. Fig. 18a and a' depict the welded joint obtained with a 4 mm initial gap between the die cross-sections. The oscillations and forging conditions were 1.5 mm at 15 Hz and a 2 mm stroke at 250 MPa pressure, respectively. Fig. 18a'' illustrates the corresponding upsets normal to and along the oscillation directions, with maximum values of about 1.25 and 2 mm, respectively. The smaller upset at a lower frequency of 15 Hz indicates insufficient plastic deformation for bonding

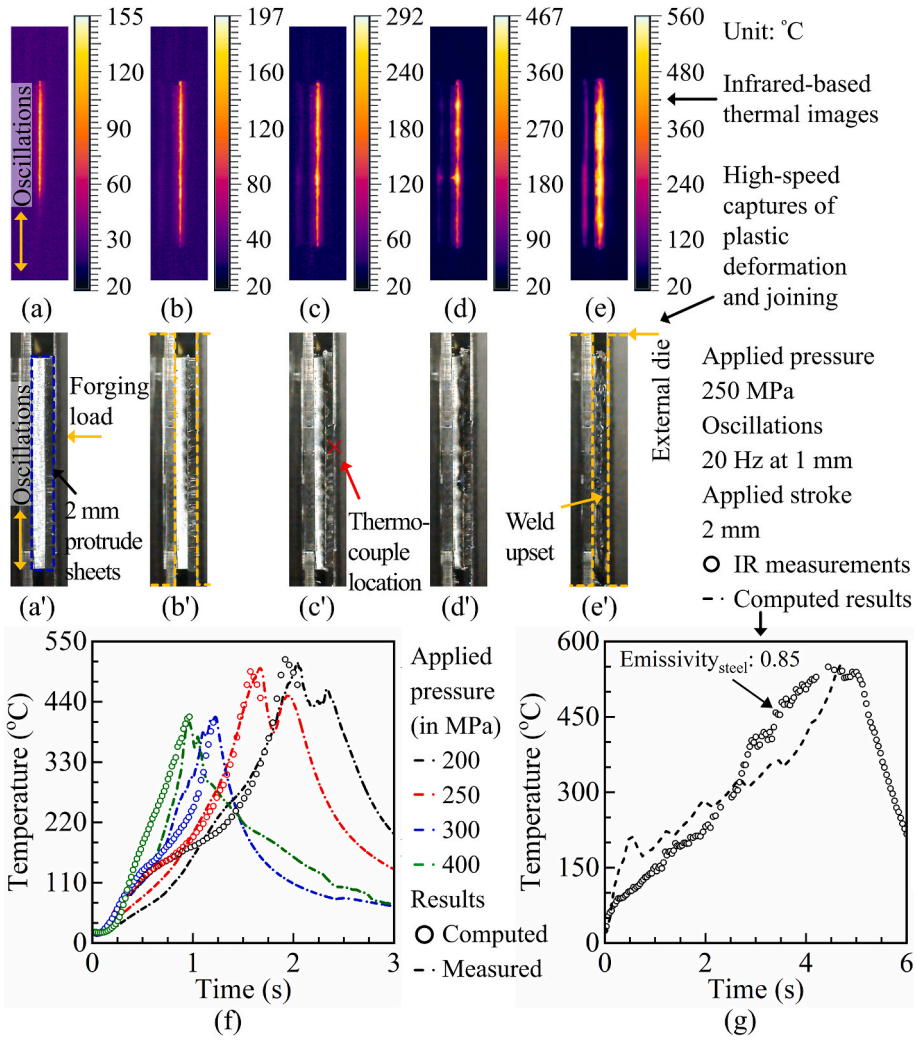

Fig. 15. Temperature and deformation monitoring. Figures show the recorded infrared-based thermal images of linear friction welding of 2-mm-thick S45C steel sheets at different time instants of (a) 0, (b) 0.2, (c) 0.7, (d) 2.7, and (e) 3.9 s and applied pressure, oscillations and stroke of 250 MPa, 1 mm at 20 Hz and 1 mm, respectively. (a' to e') denotes the corresponding high-speed captures of interfacial plastic deformation during the joint evolution under similar conditions. (f to g) reveals recorded welding temperature and their validations against the computed results. (f) plots the temperatures measured by the thermocouples at an initial distance of 1.5 mm from the interface and the applied pressures of 200–400 MPa. (g) shows the temperature measured by the infrared camera and computed under the applied pressure of 250 MPa.

(Fig. 7b and 18a'’). The larger upset in the oscillation directions signifies unsteady shear deformation at a slower speed (Fig. 18a'’). Fig. 18b and b′ display a non-uniform material ejection (distorted grey region) along the joint length. The processing conditions included an initial gap of 6 mm between the external dies, a 250 MPa applied pressure, and oscillations of 1.5 mm at 20 Hz. The forging stroke remained constant at 2 mm. A slight lateral misalignment after welding along with the inclined upsets is visible in Fig. 18b', which denotes inadequate interfacial interactions for appropriate bonding. Fig. 18b'’ illustrates the measured upsets with 1.25 and 1.5 mm peaks in the normal and oscillation directions, respectively. Fig. 18a'’ and b'’ distinguish the plastic deformation based on the upset cross-section area. After the LFW of a 3 mm protruded sheet, a wider upset base was achieved. This further indicates excessive bending and plastic deformation for large, unconstrained sheet lengths (Fig. 18b). The irregular interfacial heating (Fig. 17c and 18b) highlights the necessity to examine the requisite combinations of applied pressure, stroke, oscillations, and joint geometry to achieve high strengths through thin sheet LFW.

Fig. 19 illustrates the spatial and transient variations in the computed responses during LFW at different frequencies, amplitudes, and applied strokes. Fig. 19a shows that peak interfacial temperatures of 587 and 633 °C were obtained with oscillation amplitudes of 1 and 2 mm at 20 Hz, respectively. These values deviate from the peak of 659 °C calculated for a 1.5 mm amplitude (Fig. 14a), indicating optimal conditions. The applied pressure and stroke remained constant at 250 MPa and 2 mm. The restrained temperature increment rates with a 1 mm amplitude are intuitive. The visible serrations in temperature rise denote simultaneous oscillations and high-pressure forging strokes involving heat loss under axial compression (Fig.s. 16c and 19a). This stage in experimentation facilitated the creation of new interfaces via material ejection due to shear and normal plastic flow. This phenomenon remains challenging to model, involving continual plastic flow, and often leads to slight variations in calculations. For example, a peak temperature of 714 °C computed at a 15 Hz frequency represents an anomaly with respect to the expected temperature, which would be lower due to the generation of new interfaces. For a 1 mm stroke, 455 °C at 1.82 s illustrates the restricted plastic deformation at lower displacements and 1.5 mm oscillations at 20 Hz.

Figs. 19b and c depict similarities in the transients of interfacial upset and equivalent plastic strain. The meshed geometry on the right denotes the probe location at the interface center (for plastic stress, strain, and temperature) and the left end (for normal upset). At 15 Hz, the

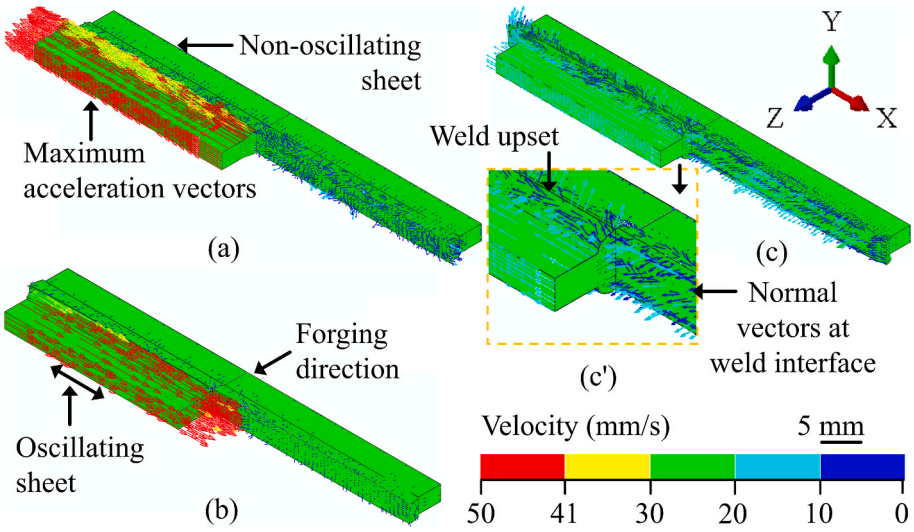

Fig. 16. Kinetics of interfacial deformation during oscillations and forging. Figures show the computed velocity vectors of joint evolution at different time instants of (a) 0.31 s, (b) 0.34 s, and (c) 0.43 s (a to c) indicates different oscillations and forging stages during linear friction welding of 2-mm-thick S45C steel sheets. (c'') The enlarged image displays axial compression and upsetting of the welded cross-section with concurrent 1.5 mm oscillations at 20 Hz.

Table 2
Process conditions of the welded specimen for tensile strength test.

S.No.	Pressure (MPa)	Stroke (mm)	Frequency (Hz)	Amplitude (mm)	Gap between dies (mm)	Processing time (s)
I	250	2	15	1.5	4	6.51
II	250	2	20	1	4	4.67
III	250	2	20	2	4	1.23
IV	250	1	20	1.5	4	1.82
V	200	2	20	1.5	6	2.18
VI	400	2	20	1.5	6	0.77

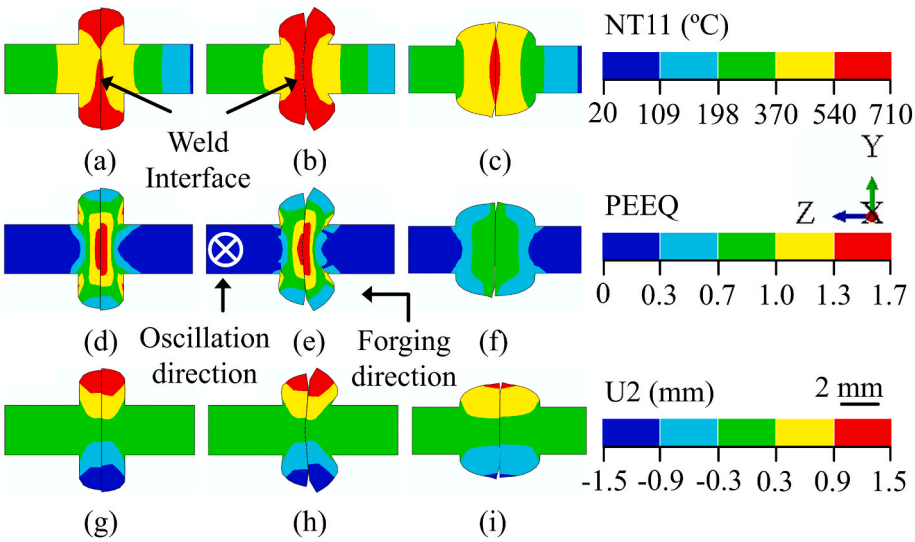

Fig. 17. Impact of weld joint designs on temperature, strain, and deformation. Computed contours of (a to c) nodal temperature, (d to f) equivalent plastic strain, and (g to i) normal interfacial upset for different weld geometries of (a, d, and g) 4 mm gap between external dies, (b, e, and h) without an external die and (c, f, and i) 6 mm gap during linear friction welding of 2-mm-thick S45C steel sheets. The applied pressure and oscillations are 200 MPa and 1.5 at 20 Hz, respectively.

maximum upset was calculated to be 1.40 mm at 6.51 s, which is slightly greater than the measured 1.25 mm (Fig. 18a''). This variation is attributed to a slightly higher estimated temperature (Fig. 19a) and is an outlier. For 1 and 2 mm amplitudes, the maximum upsets were calculated to be 1.37 and 1.49 mm, respectively, slightly lower than the 1.62 mm recorded under the 1.5 mm applied amplitude (Fig. 7b), revealing the lower calculated temperatures and suboptimal conditions (Fig. 19a). For a 1 mm stroke, the 0.63 mm upset indicates incomplete joining. The corresponding plastic strain was calculated to be 0.72 (Fig. 19c). At 1 and 2 mm amplitudes, the maximum computed plastic strains were 1.54 and 1.56, respectively. At 15 Hz, the maximum plastic strain of 1.6 indicates that the applied frequency had a greater influence than the amplitude of oscillation for the requisite plastic deformation, which merits further investigation. Fig. 19d shows the equivalent plastic stress

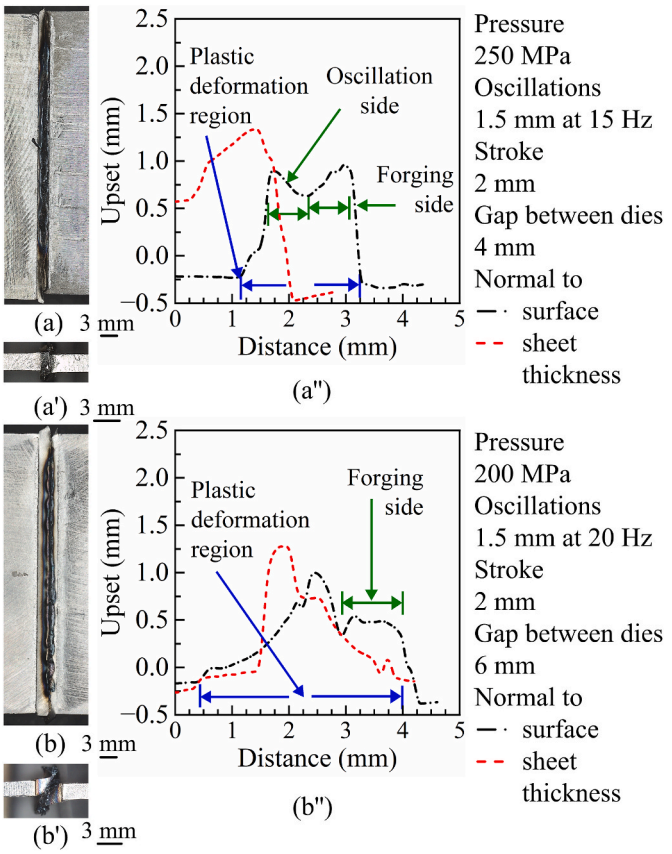

Fig. 18. Impact of initial gap and oscillation frequency on joint geometry and deformation. The figures show the welded specimen image (on the left) and measured interfacial upset dimensions (on the right) under two different conditions of (a-a'-a'') 4 and (b-b'-b'') 6 mm initial gap between external die cross-sections. The applied stroke is 2 mm, applied pressures are (a) 250 and (b) 200 MPa, and oscillation frequencies are (a) 15 and (b) 20 Hz at 1.5 mm amplitude.

distribution computed at the interface center. For a 2 mm amplitude, the stress rapidly fluctuated between 400 and 1400 MPa. For a 1 mm amplitude, stress fluctuation had a two-stage variation, i.e., between 100 to 500 MPa and 250–1400 MPa, which implies that an initial aid of generated stress is required for materializing upset at subdued oscillations. At 15 Hz, 200–1100 MPa stress variations were initially induced with trivial increments under a modest temperature rise. The subsequent fluctuations with 200–600 MPa signify the reduced plastic extrusion rate. The concentrated fluctuations within 100–700 MPa (Fig. 19d) refer to a short 1 mm forging stroke.

Figs. 19e and f elucidate the interfacial plastic flow and joining in LFW through thermal and plastic strain localization. Fig. 19e shows the peak temperatures of 659, 604, 545, and 521 °C calculated at the interface and at distances of 0.5, 1, and 1.5 mm for an applied pressure, stroke, and oscillation of 250 MPa, 2 mm, and 1.5 mm at 20 Hz, respectively. The meshed figure at the bottom displays the corresponding initial probe locations. The peak strains and temperatures during welding were observed at the end of the process and align with local plastic flow phenomena (Figs. 17, 19a and 19c). For the 1 and 2 mm amplitudes, peak temperatures vary from 511 to 587 °C and from 546 to 644 °C, respectively, at different distances. A moderate temperature fall implies a deviation in thermal localization for controlled plastic flow during the welding of thin cross-sections. The stroke of 1 mm involved a temperature distribution of 370–471 °C in the weld region and exemplifies the insufficient temperature range for joining. For the 15 Hz frequency, a mere 16 °C temperature drop in the weld region implies a rise in heat dissipation due to prolonged moderate oscillations. The plastic strain at 15 Hz was calculated to be 1.04 to 1.62 across the weld region (Fig. 19f). For similar amplitudes and a 20 Hz frequency, the maximum plastic strain range in the weld region was computed as 1.55 to 1.66. This signifies the influence of the applied forging displacement on the interfacial plastic flow besides the temperature gradient. The plastic strains for the 1 and 2 mm amplitudes (Fig. 19f) were calculated to be 1.22 to 1.54 and 1.06 to 1.56, respectively, in the welded region. For larger amplitudes, the higher plastic strain gradients indicate excessive shearing under the applied stroke of 2 mm. For the 1 mm stroke, smaller plastic strains of 0.56–0.72 were observed.

5.9. *Mechanical and microstructure features of welded joints under different conditions*

Fig. 20 shows the nominal stress and nominal strain curves and the details of maximum joint strength and elongation at break during tensile tests of linear friction welded specimens under different applied strokes, frequencies, amplitudes, and gaps between external dies. Table 2 outlines the process conditions. The maximum load/strength and elongation of 3.11 kN/262 MPa and 0.4 mm, respectively, were achieved with the welded specimen fabricated at 15 Hz (Parameter I). The tensile test (Fig. 20d) reveals a weld fracture. Fig. 20d_1 shows the brittle fractured cross-section. The lower joint strengths at smaller oscillation frequencies reflect inadequate heating and interfacial plastic deformation, leading to poor metallurgical bonding. The maximum load/strength and elongations for the 1 and 2 mm applied amplitudes (Parameters II and III) were obtained as 7.2 kN/606 MPa and 5.9 mm, and 7.19 kN/605 MPa and 6.35 mm, respectively. The ductile base metal fractures (Fig. 20b and c) with 0.2–0.3 plastic strains denote interfacial hardening. This indicates that the interfacial heating and plastic deformation under different applied amplitudes were relatively adequate for a high-strength joint. The maximum and minimum strengths were achieved at the 1.5 mm and 1 mm amplitudes, respectively, among the investigated conditions. Further, it is worth noting that the oscillation frequency had a greater influence on heat generation, material ejection, and metallurgical bond formation. Fig. 20b_1 and 20c_1 depict the fractured interfaces of tensile-tested specimens obtained at different amplitudes. The maximum joint strength for a 1 mm applied stroke (Parameter IV) was 267 MPa with a fractured welded interface, indicating incomplete plastic deformation for adequate bonding. The weld joints with a 3 mm protruded sheet, i.e., a 6 mm die gap, resulted in maximum strengths of 481 and 558 MPa for the applied pressures of 200 and 400 MPa (Parameter V and VI), respectively. The oscillations of 1.5 mm at 20 Hz were kept constant. The drop in joint strength is attributed to lateral misalignment, leading to inadequate interfacial plastic deformation for metallurgical bonding.

Fig. 21 reveals the microhardness distribution across the linear friction welded interface obtained under different conditions. The indentation pitch was mainly between 0.1 and 0.25 mm. Fig. 21a presents the microhardness distribution for the joints obtained at an applied pressure of 200–400 MPa. The maximum values were 325–347 Hv in the weld region. This indicates a slight interface hardening promoted by different mechanisms, namely martensitic strengthening and dynamic recrystallization, at 200 and 400 MPa (Fig. 9c, f, and 21a), respectively. The cementite slightly contributed to the precipitation hardening of the joints at higher applied pressures, leading to a slightly higher weld microhardness at the 400 MPa applied pressure. Similar microhardness in the weld region obtained under the applied pressures of 250 and 300 MPa (Fig. 21a) was caused by a near inter-critical deformation in alpha + gamma, which led to very fine ferrite grains together with martensite (Fig. 9d and e). The grain refinement at intermediate pressures is attributed to the deformation occurring in the inter-critical temperature range, which prohibited grain growth. A 321 Hv microhardness at a distance of 0.9 mm from the welded interface under 300 MPa applied pressure, for example, further indicates dislocation hardening in contrast to grain refinement through different mechanisms (Fig. 21a). Fig. 21b presents a higher 359 Hv microhardness in the weld region obtained at 15 Hz frequency. A 297 to 311 Hv peak microhardness in the

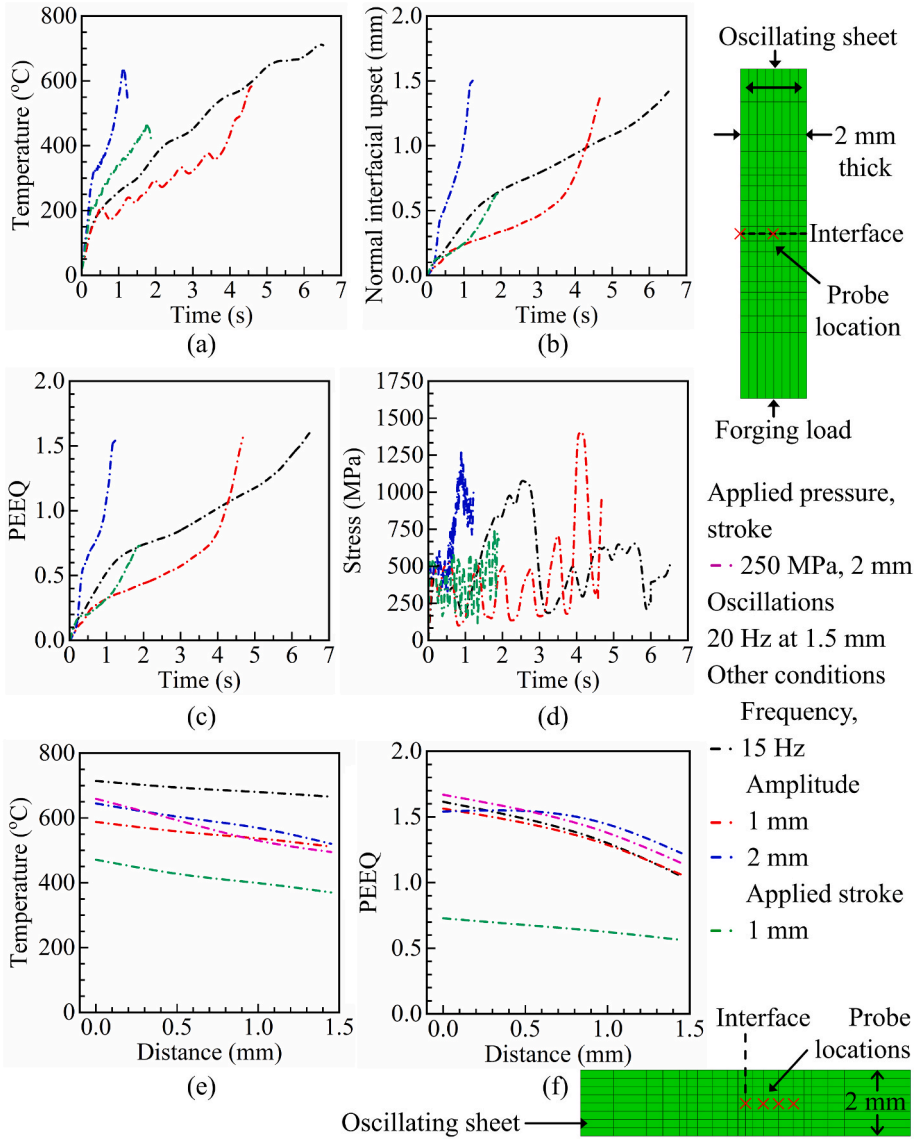

Fig. 19. Thermo-mechanical responses under varying conditions. The figures show the computed transient and spatial distribution of (a and e) nodal temperature, (b) normal interfacial upset, (c and f) equivalent plastic strain PEEQ, and (d) equivalent plastic stress during linear friction welding of 2-mm-thick S45C steel sheets. Applied pressure of 250 MPa is kept constant, and the applied stroke, frequency, and amplitudes are discreetly varied from 2 to 1 mm, 20 to 15 Hz, and 1.5 to 1 and 2 mm, respectively. The spatial variations (e and f) are obtained at the interface and 0.5, 1, and 1.5 mm distances, as indicated in the meshed figure on the right bottom. The meshed figure on the top right indicates probing locations for transient mechanical responses (a to d).

weld region was obtained with different applied amplitudes (1–2 mm) and a constant stroke (1 mm). The applied pressure was set at 250 MPa. The higher weld interface microhardness at a lower 15 Hz oscillation can be attributed to the grain refinement via lower-temperature plastic deformation (Fig. 21b). The subtle difference in the microhardness of the weld regions formed at 1 and 2 mm amplitudes shows the amplitude has a lower influence than the applied pressure, which governs the interface microstructures and hardening mechanisms. A slightly random trend in microhardness distribution at smaller forging strokes indicates inadequate heat affecting the joints following incomplete welding (Figs. 20 and 21b).

Fig. 22a shows a scanning electron microscopy image of the weld region in the linear friction welded cross-section. The welding conditions include a 250 MPa applied pressure, 2 mm stroke, and oscillations of 2 mm at 20 Hz. Fig. 22b shows the microstructure around the welded region, depicting interfacial plastic deformation and a recrystallized area in the downward region. Fig. 22c, d, and 22e depict the heat-affected area, plasticized region, and local dynamically recrystallized microstructure transitions, respectively. Figs. 22d and e shows evidence of ferrite refinement and martensitic transformation in the welded region's microstructures. Fig. 22f shows the microstructures of the welded region obtained at a 1 mm amplitude and a constant applied pressure of 250 Ma. The fine ferrites and white contrast cementite particles in Fig. 22f indicate that the peak temperature fell below the A_1 point because the amplitude was changed from 1.5 to 1.0 mm compared with the results in Fig. 9d. The computed transient in Fig. 19a and the slightly lower joint strength in Fig. 20 also indicate this lower temperature welding condition (Fig. 22f). Similar linear friction welded microstructures were observed under a 15 Hz applied frequency (Fig. 22g) and 1 mm forging stroke (Fig. 22h) at a 250 MPa pressure. These results explain the varying mechanics of microstructure development and joint formation during LFW at a constant pressure. The estimated conditions in Figs. 14a, 15f and 19a indicate almost the same welding mechanics, i.e., varying temperature conditions that promote ferrite and martensite (Figs. 9d and 22e) and fine ferrites with cementite particles (Fig. 22f, g, and 22h) during joint formation at different applied pressures,

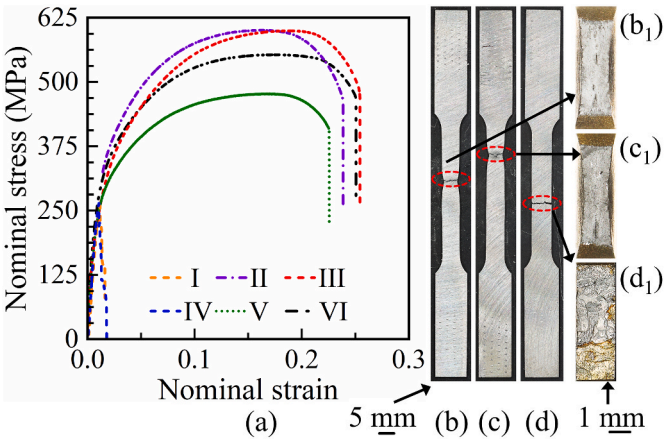

Fig. 20. Tensile test results under varying conditions. (a) Nominal stress-strain curves under different I to VI process conditions (Table 2). (b, c, and d) displays fractured tensile tested welded specimens obtained at applied (b) 1, (c) 2 mm amplitudes, and (d) 15 Hz frequency. (b_1, c_1, and d_1) macro-images of the corresponding fractured surfaces.

oscillations amplitudes, and frequencies. The applied 15 Hz frequency represents the only outlier for which the model could not simulate low-temperature, higher weld microhardness conditions (Figs. 19a, 21b and 22g). The lower joint strengths with interface fracture results (Fig. 20a, d, and 22g) further confirmed the underlying complexity of computing friction heating and plastic deformation during simultaneous high-pressure oscillations and forging strokes. Fig. 22i shows the base metal coarse ferrite and lamellar pearlite annealed microstructures for comparison.

5.10. Summary and future steps

A novel method for joining thin metallic sheets using pressure-controlled oscillations and applied displacement is presented. The results showed localized plastic yielding and metallurgical bonding, with weld temperature decreasing as the applied pressure increased. The computed results reveal material flow kinetics, with serration in temperature increments denoting axial compression during high-frequency, high-pressure oscillations. This efficiently enables high-strength solid-state joints through plastic deformation across thin-walled structures. This aspect of linear friction welding offers innovative solutions to diverse engineering material geometries. The ongoing research focuses on the experimental and numerical investigation of joining dissimilar thin materials for automotive applications involving asymmetrical heat generation and plastic deformation at the welding interfaces. The subsequent challenge is to produce dissimilar joints with varying thicknesses, leading to increased uncontrolled plastic flow during joint formation. The current technique's key advantage is its intermittent axial compression during oscillation-based frictional heating at constant pressure, effectively preventing uncontrolled extrusion of thermally softened interfaces. Moreover, the concept of adjusting maximum welding temperature with applied pressure relative to material yield strength enhances process feasibility for various engineering applications. However, the complex weld design needed for clamping large sheet volumes slightly limits the current solution. To advance this work for industrial and academic applications, a more robust external die design that ensures precise pressure and mechanical motion is essential. Achieving this will enhance the relevance of this research, and an investigation is currently underway.

6. Conclusions

The following conclusions are drawn from the integrated numerical and experimental investigations on the linear friction welding of 2-mm-thick S45C steel sheets under different process conditions.

1. Linear friction welding of metallic sheets is challenging and is successfully achieved through controlled plastic deformation of the interfaces under simultaneous oscillations and forging stroke while maintaining high applied pressure.
2. Numerical and experimental investigations successfully demonstrate how increasing the pressure, for example, from 200 to 400 MPa, reduces the welding temperature from about 696 to 614 °C. This information is beneficial for successfully achieving the controlled interfacial plastic deformation in linear friction welding of thin cross-section S45C and other high-strength steel sheets.
3. External die blocks clamp large sheet volumes, controlling oscillations, local plastic flow, and forging in 2–3 mm protruded sheet

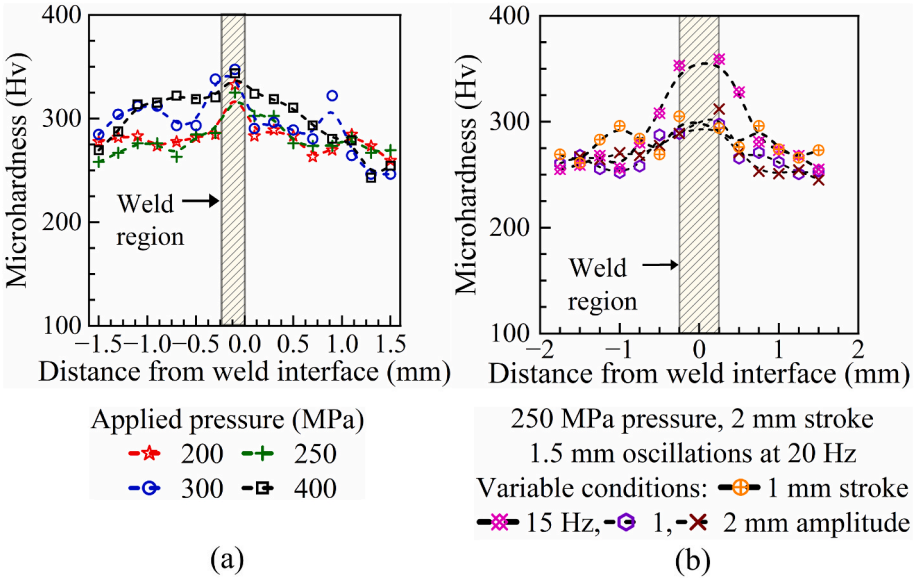

Fig. 21. Microhardness of linear friction welded joints. (a) shows microhardness distribution across the welded interface under different applied pressures of 200–400 MPa. The applied stroke of 2 mm and oscillations of 1.5 mm at 20 Hz are set constant. (b) shows microhardness distribution at set 250 MPa applied pressure and varying conditions of applied stroke (1 mm), amplitudes (1 and 2 mm), and frequency (15 Hz).

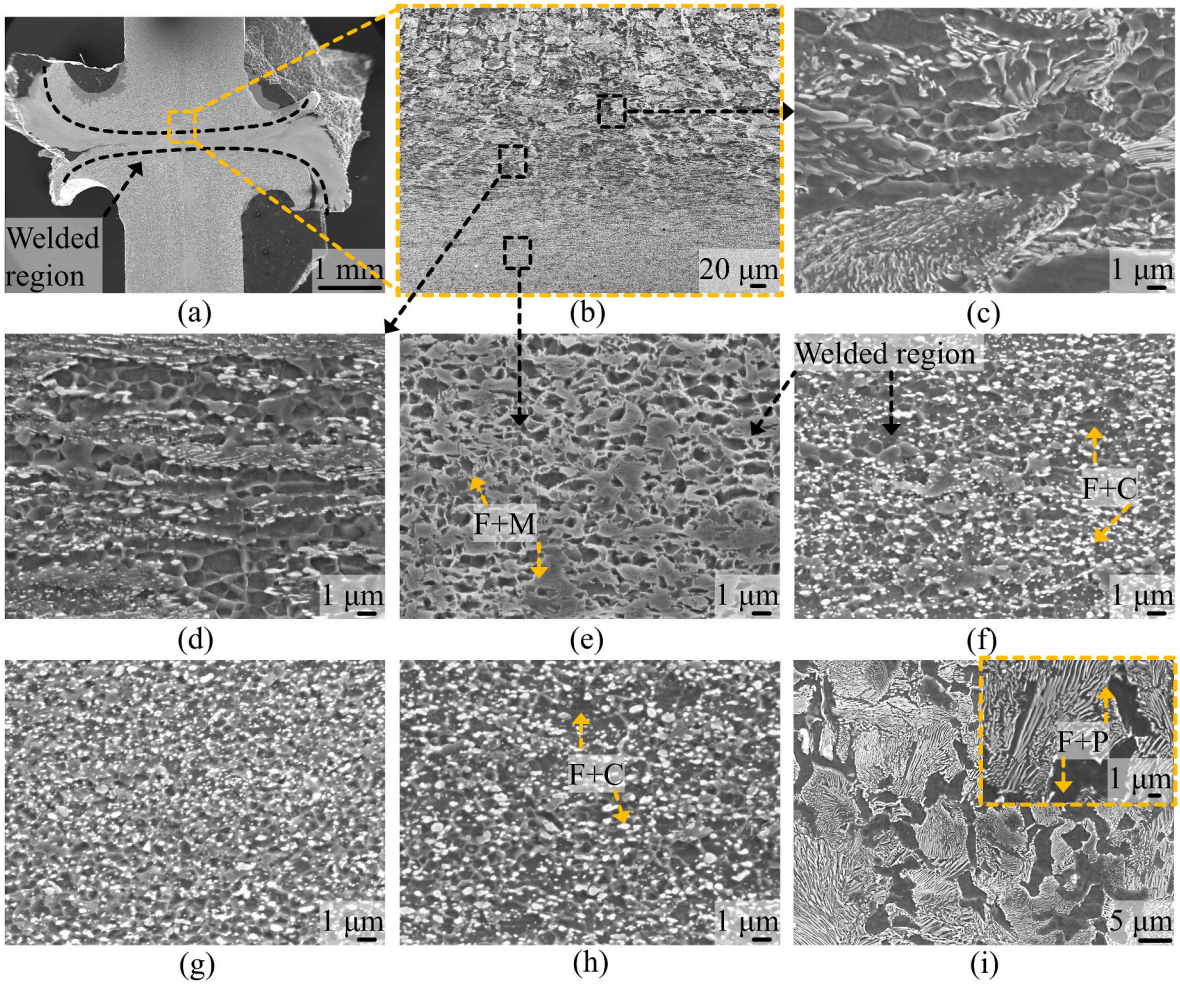

Fig. 22. Microstructural evolution in linear friction welding under varying conditions (a) shows joint cross-section and welded region at 20× magnification, (b) shows gradient microstructure distribution across the weld boundary denoted by a yellow rectangular box. The applied pressure is 250 MPa, oscillation is 2 mm at 20 Hz, and stroke is 2 mm. (c, d, and e) shows microstructures at different distances from the welded interface at 2000× magnification. The other microstructures in (f, g, and h) show the welded region obtained under variable conditions of applied (f) 1 mm amplitude, (g) 15 Hz oscillation frequency, and (h) 1 mm stroke. (i) shows base metal microstructures. (For interpretation of the references to color in this figure legend, the reader is referred to the Web version of this article.)

sections. A narrower initial gap in the external die design prevents lateral misalignment and unwanted plastic upset, enhancing joint strength and increasing its feasibility for use in other materials.

4. The maximum strength and base metal fracture in thin sheet joints occur under oscillations and strokes of 1.5 mm at 20 Hz and 2 mm, respectively, under 200–400 MPa pressures. An applied pressure of 250 MPa results in fractures farthest from the weld interface. Variations in these conditions caused inadequate heating, plastic flow, and decreased weld strength in $2 \times 50\ mm^2$ S45C steel cross-sections.
5. In linear friction welding, increasing the applied pressure from 200 to 400 MPa shifts the strengthening mechanism from martensitic strengthening to grain refinement strengthening in the S45C steel interface. The peak welding temperature drops below the A_1 point and the large fraction of martensite microstructures changes to very fine ferrites with extremely small, fragmented cementite particles due to the dynamic recrystallization.
6. Novel modeling of interfacial plastic deformation and external die interactions via coupled thermal-stress analysis reveals an elliptical thermal distribution indicating low friction in upset-out material. Further insights into alternating interfacial plastic stress and strain reveal material flow kinetics under simultaneous pressure-controlled oscillations and forging displacements.
7. Both the interfacial temperature and upset during the linear friction welding of 2-mm-thick S45C steel sheets increase with the oscillations and forging. Higher pressures promote consistent increments, slight asymmetrical plastic flow, and edge-thinning under higher compression rates. The computed serrations in the temperature increments confirm the occurrence of axial compression during oscillation-based frictional heating.

CRediT authorship contribution statement

Rishabh Shotri: Writing – original draft, Validation, Software, Methodology, Investigation, Formal analysis, Data curation, Conceptualization. **Takuya Miura:** Writing – review & editing, Investigation. **Peihao Geng:** Investigation, Formal analysis. **Yoshiaki Morisada:** Writing – review & editing, Supervision, Project administration, Funding acquisition, Conceptualization. **Kohsaku Ushioda:** Writing – review & editing, Visualization, Supervision, Conceptualization. **Hidetoshi Fujii:** Writing – review & editing, Supervision, Project administration, Funding acquisition, Conceptualization.

Declaration of competing interest

The authors declare no known competing financial interests or personal relationships that could have appeared to influence the work reported in this paper.

Acknowledgments

This work was supported by the JST-Mirai Program Grant Number JPMJMI19E5 and JSPS KAKENHI Grant Number JP19H00826 and JP23K13576.

Appendix A. Supplementary data

Supplementary data to this article can be found online at https://doi.org/10.1016/j.ijmachtools.2024.104235.

Data availability

Data will be made available on request.

References

[1] Z. Guo, T. Ma, X. Yang, W. Li, Q. Xu, Y. Li, J. Li, A. Vairis, Comprehensive investigation on linear friction welding a dissimilar material joint between Ti17 (α + β) and Ti17 (β): microstructure evolution, failure mechanisms, with simultaneous optimization of tensile and fatigue properties, Mater. Sci. Eng. (2024) 146818.
[2] A.R. McAndrew, P.A. Colegrove, C. Bühr, B.C. Flipo, A. Vairis, A literature review of Ti-6Al-4V linear friction welding, Prog. Mater. Sci. 92 (2018) 225–257.
[3] T. Ito, M. Kamai, T. Miura, Y. Morisada, H. Fujii, Dissimilar joining of carbon steel, pure nickel and aluminum alloys by center-driven double-sided linear friction welding, Journal of Advanced Joining Processes (2023) 100165.
[4] S. Tabaie, F. Rézaï-Aria, B.C. Flipo, M. Jahazi, Dissimilar linear friction welding of selective laser melted Inconel 718 to forged Ni-based superalloy AD730™: evolution of strengthening phases, J. Mater. Sci. Technol. 96 (2022) 248–261.
[5] X. Yang, S. Ma, Q. Chu, C. Peng, Y. Su, B. Xiao, Z. Guo, T. Ma, W. Li, Investigation of microstructure and mechanical properties of GH4169 superalloy joint produced by linear friction welding, J. Mater. Res. Technol. 24 (2023) 8373–8390.
[6] P. Zhao, Y. Tao, H. Chen, Y. Hu, Q. Chu, M. Zhang, Y. Li, N. Ma, J. Tao, Texture characteristics and fracture mechanism of linear friction welded joints of dissimilar titanium alloys after annealing, Mater. Sci. Eng. 866 (2023) 144709.
[7] Y. Su, W. Li, X. Wang, T. Ma, L. Ma, X. Dou, The sensitivity analysis of microstructure and mechanical properties to welding parameters for linear friction welded rail steel joints, Mater. Sci. Eng. 764 (2019) 138251.
[8] C. Liu, Y. Gao, X. Li, W. Li, K. Gan, Study on microstructure and mechanical property of linear friction welding on 9Cr reduced activation ferrite/martensite steel, J. Nucl. Mater. 531 (2020) 152011.
[9] D.S. Lachowicz, C. Bennett, D.A. Axinte, S. Lowth, A. Walpole, C. Hannon, On the influence of tooling behaviour over axial shortening mechanisms in linear friction welding of titanium alloys and modelling plasticisation effects, Int. J. Mach. Tool Manufact. 161 (2021) 103674.
[10] A. Lis, H. Mogami, T. Matsuda, T. Sano, R. Yoshida, H. Hori, A. Hirose, Hardening and softening effects in aluminium alloys during high-frequency linear friction welding, J. Mater. Process. Technol. 255 (2018) 547–558.
[11] R. Toramoto, T. Yamashita, K. Ushioda, T. Omura, H. Fujii, Hydrogen embrittlement susceptibility of linear friction welded medium carbon steel joints, ISIJ Int. 64 (7) (2024) 1185–1196.
[12] L. Fratini, G. Buffa, D. Campanella, D. La Spisa, Investigations on the linear friction welding process through numerical simulations and experiments, Mater. Des. 40 (2012) 285–291.
[13] J.W. Choi, W. Li, K. Ushioda, H. Fujii, Flat hardness distribution in AA6061 joints by linear friction welding, Sci. Rep. 11 (1) (2021) 11756.
[14] C. Mukundhan, P. Sivaraj, V. Balasubramanian, T. Sonar, V. Petley, S. Verma, Effect of friction pressure on microstructure and tensile properties of linear friction welded Ti–6Al–4V alloy joints, International Journal of Lightweight Materials and Manufacture 6 (4) (2023) 483–493.
[15] J.W. Choi, Y. Aoki, K. Ushioda, H. Fujii, Linear friction welding of Ti-6Al-4V alloy fabricated below β-phase transformation temperature, Scripta Mater. 191 (2021) 12–16.
[16] M. Javidikia, M. Sadeghifar, H. Champliaud, M. Jahazi, Grain size and temperature evolutions during linear friction welding of Ni-base superalloy Waspaloy: simulations and experimental validations, Journal of Advanced Joining Processes 8 (2023) 100150.
[17] Z. Guo, T. Ma, X. Chen, X. Yang, J. Tao, J. Li, W. Li, A. Vairis, Interfacial bonding mechanism of linear friction welded dissimilar Ti2AlNb–Ti60 joint: grain intergrowth induced by combined effects of dynamic recrystallization, phase transformation and elemental diffusion, J. Mater. Res. Technol. 24 (2023) 5660–5668.
[18] X. Yang, W. Li, Y. Fu, Q. Ye, Y. Xu, X. Dong, K. Hu, Y. Zou, Finite element modelling for temperature, stresses and strains calculation in linear friction welding of TB9 titanium alloy, J. Mater. Res. Technol. 8 (5) (2019) 4797–4818.
[19] K. Yonekura, T. Shinohara, K. Masaki, Cost-effective estimation of flash extrusion and defects in linear friction welding using Voronoi diagrams, J. Manuf. Process. 68 (2021) 158–167.
[20] X. Liu, M. Liang, Q. Luo, Innovative electric vehicle body design based on insurance institute for highway safety side impact conditions, Automotive Innovation 2 (3) (2019) 201–211.
[21] R. Owsiński, D.S. Lachowicz, C.T. Lachowicz, R. Gil, A. Niesłony, Characterisation of joint properties through spatial mapping of cracks in fatigue specimens, extracted from the linearly friction welded steel coupon, Precis. Eng. 71 (2021) 78–89.
[22] M.R. Kelly, S.R. Schmid, D.C. Adams, J. Fletcher, R. Heard, Experimental investigation of linear friction welding of AISI 1020 steel with pre-heating, J. Manuf. Process. 39 (2019) 26–39.
[23] Y. Wang, S. Tsutsumi, T. Kawakubo, H. Fujii, Microstructure, mechanical properties and fatigue behaviors of linear friction welded weathering steels, Int. J. Fatig. 159 (2022) 106829.
[24] R. Kuroiwa, H. Liu, Y. Aoki, S. Yoon, H. Fujii, G. Murayama, M. Yasuyama, Microstructure control of medium carbon steel joints by low-temperature linear friction welding, Sci. Technol. Weld. Join. 25 (1) (2019) 1–9.
[25] R. Gadallah, S. Tsutsumi, Y. Aoki, H. Fujii, Investigation of residual stress within linear friction welded steel sheets by alternating pressure via X-ray diffraction and contour method approaches, J. Manuf. Process. 64 (2021) 1223–1234.
[26] Y. Aoki, R. Kuroiwa, H. Fujii, G. Murayama, M. Yasuyama, Linear friction stir welding of medium carbon steel at low temperature, ISIJ Int. 59 (10) (2019) 1853–1859.
[27] C. Bühr, P.A. Colegrove, A.R. McAndrew, A computationally efficient thermal modelling approach of the linear friction welding process, J. Mater. Process. Technol. 252 (2018) 849–858.
[28] P. Geng, H. Ma, M. Wang, G. Qin, J. Zhou, C. Zhang, Y. Ma, N. Ma, H. Fujii, Dissimilar linear friction welding of Ni-based superalloys, Int. J. Mach. Tool Manufact. 191 (2023) 104062.
[29] D. Baffari, G. Buffa, D. Campanella, L. Fratini, F. Micari, Single block 3D numerical model for linear friction welding of titanium alloy, Sci. Technol. Weld. Join. 24 (2) (2019) 130–135.
[30] P.D.S. Effertz, F. Fuchs, N. Enzinger, The influence of process parameters in linear friction welded 30CrNiMo8 small cross-section: a modelling approach, Sci. Technol. Weld. Join. 24 (2) (2019) 121–129.
[31] A.R. McAndrew, P.A. Colegrove, B.C. Flipo, C. Bühr, 3D modelling of Ti–6Al–4V linear friction welds, Sci. Technol. Weld. Join. 22 (6) (2017) 496–504.
[32] P. Jedrasiak, H.R. Shercliff, Modelling of heat generation in linear friction welding using a small strain finite element method, Mater. Des. 177 (2019) 107833.
[33] P. Geng, G. Qin, H. Ma, J. Zhou, C. Zhang, N. Ma, Numerical modelling on the plastic flow and interfacial self-cleaning in linear friction welding of superalloys, J. Mater. Process. Technol. 296 (2021) 117198.
[34] P. Geng, G. Qin, C. Li, H. Wang, J. Zhou, Study on the importance of thermo-elastic effects in FE simulations of linear friction welding, J. Manuf. Process. 56 (2020) 602–615.
[35] P. Geng, G. Qin, J. Zhou, Z. Zou, Finite element models of friction behaviour in linear friction welding of a Ni-based superalloy, Int. J. Mech. Sci. 152 (2019) 420–431.
[36] S.I. Okeke, N.M. Harrison, M. Tong, Computational modelling of dynamic recrystallisation of Ni-based superalloy during linear friction welding, Int. J. Adv. Des. Manuf. Technol. (2022) 1–24.
[37] G. Buffa, D. Campanella, S. Pellegrino, L. Fratini, Weld quality prediction in linear friction welding of AA6082-T6 through an integrated numerical tool, J. Mater. Process. Technol. 231 (2016) 389–396.
[38] T. Ma, Z. Guo, X. Yang, J. Jin, X. Chen, J. Tao, W. Li, A. Vairis, L. Yu, Plastic flow and interfacial bonding behaviors of embedded linear friction welding process: numerical simulation combined with thermo-physical experiment, Chin. J. Aeronaut. (2024), https://doi.org/10.1016/j.cja.2023.12.034.
[39] X. Yang, T. Meng, Q. Chu, Y. Su, Z. Guo, R. Xu, W. Fan, T. Ma, W. Li, A review of linear friction welding of Ni-based superalloys, Int. J. Miner. Metall. Mater. 31 (6) (2024) 1382–1391.
[40] R. Shotri, T. Ogura, P. Geng, Y. Morisada, K. Ushioda, H. Fujii, Numerical and experimental investigation of pressure-controlled joule-heat forge welding of steel tubes, J. Manuf. Process. 106 (2023) 240–253.
[41] R. Shotri, T. Miura, P. Geng, Y. Morisada, K. Ushioda, H. Fujii, Probing joining mechanism of Ti6Al4V-SS316L steel rods in pressure-controlled joule-heat forge welding, J. Mater. Process. Technol. 326 (2024) 118315.
[42] Abaqus Inc., Abaqus Documentation, Version 6.13, Providence, Dassault Systèmes SIMULIA Corporation, 2013.
[43] P. Geng, G. Qin, L. Chen, J. Zhou, Z. Zou, Simulation of plastic flow driven by periodically alternating pressure and related deformation mechanism in linear friction welding, Mater. Des. 178 (2019) 107863.
[44] M. Maalekian, Friction welding–critical assessment of literature, Sci. Technol. Weld. Join. 12 (8) (2007) 738–759.
[45] F. Khan, T. Miura, T. Ito, Y. Morisada, K. Ushioda, H. Fujii, Sound dissimilar linear friction welding of A7075-T6 Al and mild steel by simultaneous interfacial deformation using higher forging speed, J. Manuf. Process. 109 (2024) 512–523.
[46] ASME, ASME SA-370: Standard Test Methods and Definitions for Mechanical Testing of Steel Products, ASME, New York, 2016. Available at: www.metalspiping.com.
[47] Y. Su, X. Yang, T. Meng, X. He, D. Wu, W. Li, S. Yin, Strengthening mechanism and forming control of linear friction welded GH4169 alloy joints, Chin. J. Aeronaut. 37 (2024) 609–626.